

Dear Michal Malinowski,

we thank you and the two anonymous reviewers for the thoughtful review of our manuscript. The constructive comments helped us to further improve the manuscript.

We edited the manuscript carefully and addressed all comments of both reviewers. Please find below the detailed reply to the comments of the first reviewer followed by the reply to the comments of the second reviewer.

All reviewer comments are shown and highlighted as bold text, followed by our answers as indented normal text. Line numbers in our response refer to the tracked revised manuscript which is attached after our point-by-point response.

Please find also attached at the end of this document, the description of our data publication with further details about the seismic catalog reprocessing and its properties. This data publication document will be available with the seismic data catalog through GFZ data services: <http://dataservices.gfz-potsdam.de/portal/> as a separate data publication.

We appreciate your time and hope that our revised manuscript now qualifies for publication in Solid Earth.

Yours sincerely,

Maria Leonhardt, on behalf of all co-authors

## **Response to reviewer #1 comments: se-2020-139-RC1**

### General comments of reviewer #1

**1) The manuscript "Seismicity during and after stimulation of a 6.1 km deep Enhanced Geothermal System in Helsinki, Finland" brings an extended results of processing the seismic monitoring data set obtained during the hydraulic stimulation carried out in 2018. Data from different available seismic stations were combined to extend the number of detected and located events and to display the seismic moment release in time. Cross correlation technique was used to estimate focal mechanisms of the largest possible number of events whose variability was analyzed and used to determine the stress field components. The instability of fault planes was then used to assess the most prominent faults. The study deals with very interesting data on injection induced seismicity in a unique experiment and gives some valuable results. These are in particular the extended catalog, the focal mechanisms and principal stresses. Providing these data to the scientific community will undoubtedly help better understanding the induced seismicity in geothermal projects in hard rocks. However, despite of reasonable language (as I can assess as non-native speaker), the study is not easy to read. This holds e.g. to the parts on catalog methodology and results, which is not easy to understand. One of the reasons is structuring the paper to Methodology and Results sections. It is a good approach in general, but in some cases it breaks the individual topics and makes the paper longer and understanding more difficult. So I recommend to describe only the more sophisticated methods like 2.3, 2.3 and the location part of 2.1.**

#### Authors:

Thank you, we followed your suggestion and focused for the Methodology part only on the location paragraphs of 2.1, on section 2.3 and also on section 2.4 (we assume that

this is meant under the second "2.3" in the comment). Nevertheless, we decided not to exclude the first paragraph of the Methodology part (lines 94-101) because it is a short overview of the stimulation and an introduction to the section. To not describe the seismic catalog with too much detail (as mentioned in comment #12 below) and also to avoid repetition with the Results part we deleted the second and third paragraph from the Methodology.

A description of the seismic catalog, especially its reprocessing and its properties, has now been moved to the data publication to keep the manuscript more focused on the seismological study. Finally, we added the following short explanation in lines 102-106:

*"The reprocessed seismic catalog with description of its properties is available as separate data publication (see section data availability) and consists of 5,456 events that were detected and located during and after the stimulation (industrial monitoring) and reprocessed in our study. A total of 55,707 smaller events were further detected during and after the stimulation but were not located or processed later on. These were also included in published seismic catalog. For further explanation about the original seismic catalog see Kwiatek et al. (2019)."*

We also excluded the entire section 2.2 from the Methodology part, but added the last two sentences of this section as an introduction to section 3.3 in the Results (lines 292-294):

*"For the spatial distribution of the seismic moment, the area around the injection well was separated into horizontal bins of 50x50 m. The cumulative seismic moment of all events within each bin was then investigated by disregarding the depth."*

To still mention the numbers of absolute and relocated stimulation and post-stimulation events included in the catalog, we modified the following sentence in lines 120-122:

*"The enhanced sub-catalog of 5,456 events including 946 post-stimulation events was reprocessed applying a new updated 1D layered velocity model developed from P-wave onset times of calibration shots obtained during a post-injection VSP campaign (Fig. S1, see also data publication)."*

Lastly, we also updated the numbers of events included in the catalog in lines 132-138:

*"A total of 2,958 reprocessed events were absolute located around the injection well OTN-3 at an epicentral distance of less than 5 km and at depth of 4.5 to 7 km. The hypocenters of these events were included to the reprocessed and published catalog.*

*To further refine the quality of hypocenter locations, 2,178 from the 2,958 absolute located events with at least 10 P-wave and 4 S-wave picks were selected and the double-difference relocation technique (hypoDD) was applied using the new VSP-derived velocity model (Waldhauser and Ellsworth, 2000)."*

We hope that these changes help to improve the understanding and simplify the reading of the paper.

**2) I also think that the spectrum of methods applied is too wide with no clear focus. The authors should decide if they present new high quality extensive seismic catalog whose parameters are characterized by a set of suitable (statistical) methods or they present a seismological study including interpretations. The point is that despite the catalog is the most valuable output, it is never characterized by at least Gutenberg-Richter distribution and similar methods.**

Authors:

We decided to keep the description of the new catalog to minimum and shift discussion on its preparation to the separate data publication (please see the data publication document attached at the end of our responses). In consequence, the methodology and processing parts of the manuscript were streamlined, and we focused our analysis on the source mechanisms and mechanisms complexities, so we now believe the focus of the manuscript was sharpened.

**3) The authors also spent a lot of effort determining focal mechanisms using quite sophisticated method to get maximum number of mechanisms, they however do not show the whole set of FM and assess their quality.**

Authors:

The quality of focal mechanisms was assessed by the root mean square fault plane uncertainties of the estimated focal mechanisms (Hardebeck and Shearer, 2002). We only further investigated focal mechanisms which had uncertainties less or equal 35°, as suggested by Hardebeck and Shearer (2002). Focal mechanisms with associated uncertainties are a part of the data publication, and we indicated this in the text in lines 196-198:

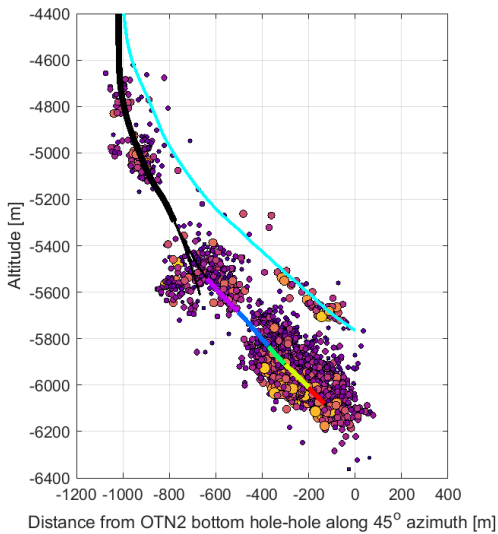
*"The final catalog of focal mechanisms includes 191 events with either manually or estimated polarity pattern and is presented with associated uncertainties in the data publication (see section data availability)."*

**4) I am also not sure about the improved quality of locations in terms of their asymmetric position to the borehole.**

Authors:

The asymmetric distribution of hypocenter locations to the borehole is indeed interesting, but we are at the moment very confident that this is the case. This is supported by two independent analyses, one conducted by the main Author and one being a part of new study by Kwiatek et al. (2021).

We identified that the position of the cluster is affected predominantly by the assumed  $V_p/V_s$  ratio. Thus, as the positioning of the cluster was vital for the interpretation of the seismicity, we optimized the cluster position using two criteria: 1) the sum of residuals for all events from location procedure should be minimal, and 2) hypocenters of events at the beginning of stimulation should occur in direct vicinity of injection interval. Our analysis, as presented in submitted manuscript, resulted in  $V_p/V_s$  ratio optimized to 1.67 (which is not very different from 1.68 assumed in Kwiatek et al., 2019). However, we updated  $V_p/V_s$  ratio to 1.71 using new seismic catalog obtained during 2020 stimulation in OTN-2 well (which is a subject of a pending study of Kwiatek et al., 2021). The new defined constrain was that 3) events from 2020 stimulation should cluster around OTN-2 well. The final outcome of locations is shown in the Figure below (however, we restrain from presenting 2020 stimulation data in SE manuscript, as this is a part of pending study).



The revised manuscript uses now hypocenters estimated with a  $V_P/V_S$  of 1.71. We updated our seismic data catalog.

Using the higher ratio of 1.71, the hypocenters of the 2018 induced events are shifted approximately 300 m upwards in depth. With this shift in depth, the hypocenters are also now more symmetrically located around the injection well, as shown in the revised manuscript (updated Fig. 3a-b). Because of minor changes in takeoff angles, no significant change in focal mechanisms was observed.

We also updated the following sentence in lines 123-126:

*"Thus, the  $V_P/V_S$  ratio was optimized by a trial-and-error procedure, where we ultimately constrained a  $V_P/V_S$  ratio of 1.71 that minimized the cumulative residual errors of all located events, and at the same time kept the first induced events close to corresponding injection well OTN-3."*

**5) As a result I believe the paper should be restructured according to its main focus - presentation of new data. Details of my comments which should be addressed in a major revision are summarized below.**

Authors:

We restructured the manuscript, especially the Methodology and Results parts (for the results, please see the response to comment #12), to focus on the seismological study while keeping the development and properties of the catalog to the minimum. Associated data publication (please see the attached document at the end) contains relevant information on how the catalog was designed and catalog properties.

Particular comments of reviewer #1

**6) Ln 109-120 (Methodology). The explanation about different subsets of larger and smaller events and their relocation is not very clear. E.g. how many events were above Mw 0.7; were the 3464 events chosen from this subset?; did these events occur during stimulation because you added 321 post-stim events?; did 68 events com from this subset?...**

Authors:

With updating our seismic catalog using now a  $V_P/V_S = 1.71$ , we also simplified the selection of events used for reprocessing, especially not distinguishing between subsets of larger and smaller events anymore. The reprocessing steps and details about the seismic catalog and its statistical properties are now part of the data publication.

**7) Ln 172 - 176. Please explain the SVD application in more detail. The point is that SVD is usually used to find a common pattern in a data set. For this you would need more polarity patterns for each event that just one, which you have as a result of cross correlation. The next question is whether the polarity matrix (eq. 2) shows the polarity fit between the target and template events as indicated on Ln 171 or the fit of polarities themselves. In the first case, it could not be used for calculating focal mechanisms.**

Authors:

Indeed, the SVD is usually used to find a common pattern in a data set and this is also the reason why we applied the SVD. The method of Shelly et al. (2016) is a well-established approach where the SVD is applied to extract a common polarity signal from a matrix that contains the obtained relative polarities between each target events and all template events, considering each station and phase (in our case only P-phase) separately.

For each station, the left singular vector is obtained by applying the SVD to the above mentioned matrix. This vector provides a means of estimating the most consistent set of polarities (sign of the elements) for each target event and station (Shelly et al., 2016).

In our manuscript, the left singular vectors of all stations are presented in the columns of the matrix in equation 2. Therefore, only the most reasonable polarity for each target event and each station is presented in equation 2 as a best fit of many relative polarities derived from cross-correlation between this target event and many templates. Thus, the best fit for each target event still shows a polarity ambiguity. This sign ambiguity of polarities can only be resolved later on when considering the manually picked polarities of some target events.

We restrain from describing the methodology in manuscript in details, as this is a subject of Shelly et al. (2016) where the method is described in details in step-by-step fashion.

We added the following sentence to the manuscript in lines 180-181:

*"For each station  $k$ , the vectors containing relative polarity estimates between one target event  $i$  and all templates  $j$  were gathered in a  $i$ -by- $j$  matrix."*

We further rewrote the following sentence in lines 182-185:

*"A Singular Value Decomposition (SVD) was applied to the relative estimated polarity matrix of each station  $k$  to extract the strongest common signal of any target event obtained by the first left singular vector of the SVD (Shelly et al., 2016; Rubinstein and Ellsworth, 2010)."*

**8) Ln 178. The way you reduced the polarity ambiguity is not clear; by considering manually picked events one can verify the automatic picks, I believe.**

Authors:

This is precisely what we have performed. Manually picked events and their “true” polarities were used to resolve the ambiguity of SVD-derived polarities for all events at each station, separately. If the SVD-derived polarities has the same sign as the manually picked polarities for one station, than all automatically derived polarities of the other events should also have the right polarities for this particular station due to the first singular vector of the SVD.

We updated the following part of the manuscript (lines 190-192):

*"For each station, the SVD-derived polarities of these events were compared with manually picked polarities to investigate whether the polarities have similar or opposite signs. In case of same polarities, the SVD-derived polarities of other events should also show the right sign for the particular stations."*

**9) Ln 185. The final sentence mentioning the resulting reverse faulting fits rather to the Results than Methodology section.**

Authors:

Yes, we agree. We deleted this sentence at the end of our Methodology section.

**10) Ln 195. Please argue for using this distance metrics - what is the reason for 1.5 in the denominator? And which type of cluster analysis did you use? What is the difference to the published method of moment tensor clustering of Cesca (2014)?**

Authors:

The choice of 1.5 is only to scale the value to range 0-1 (as the Kagan rotation angle  $\theta$  ranges  $0^\circ$ - $120^\circ$ , our distance metrics  $PR_{ij}$  scale from 0 to 1). The cosine was used to rescale Kagan rotation angles and to emphasize large differences in  $\theta$ . We found for our dataset that this choice does not influence the discussed clustering outcome (i.e. one could use distance metrics based on the Kagan angle  $\theta$  alone).

As stated in the manuscript, we used well-established hierarchical cluster analysis with distance measured using average distance (Unweighted average distance, UPGMA) and Euclidean distance metrics. The selection of particular distance metrics between clusters was made objectively using the one with highest value of the cophenetic correlation coefficient. Cesca et al. (2014) applied a density-based clustering technique *DBSCAN* (Ester et. al, 1996). Clusters can be identified as densely populated “areas” with a much higher number of points than outside of a presumable cluster. Cesca’s approach is more general, as it can be used for non-DC sources. However, in case of pure DC moment tensors, a distance metric based on the Kagan angle alone is used by Cesca et al. (2014), which is comparable to our case.

**11) Ln 209-216 (Results). I think that the VSP based model deserves more attention. The present way is not appropriate - to show the model as a result without any more details. If it is considered as a result of this study, the data, methods and results should be shown. In the opposite case, the VSP model can be cited from a different study or as a personal communication from its author.**

Authors:

Following Reviewer suggestion, we separated detailed description on catalog development from mechanism complexity analysis. We added details about the VSP velocity model build-up to the data publication. In manuscript we switched Fig. 1 with Fig. S1, as suggested in comment #20. We also added the following sentences to the caption of the new Fig. S1:

*"The VSP-derived velocity model shows a velocity inversion between 3 and 6 km depth. Below this velocity inversion, a constant velocity of 6 km s<sup>-1</sup> is suggested from sonic logs which were used for velocity estimation between 5.1 km and 6.4 km depth."*

**12) Ln 218-... The description of seismic catalog update appears too detailed and technical and overlaps with the similar section in Methodology. Please consider unifying, making it more clear and concise. Another point concerning locations is the (mis)fit of the hypocenters with the borehole trace. In the depth sections of Fig. 3 it appears that most hypocenters lie below the borehole trace, which is rather unlikely. Please compare e.g. Fig. 3 in Kwiatek et al (2019) where the hypocenters occur almost symmetrically around the borehole.**

Authors:

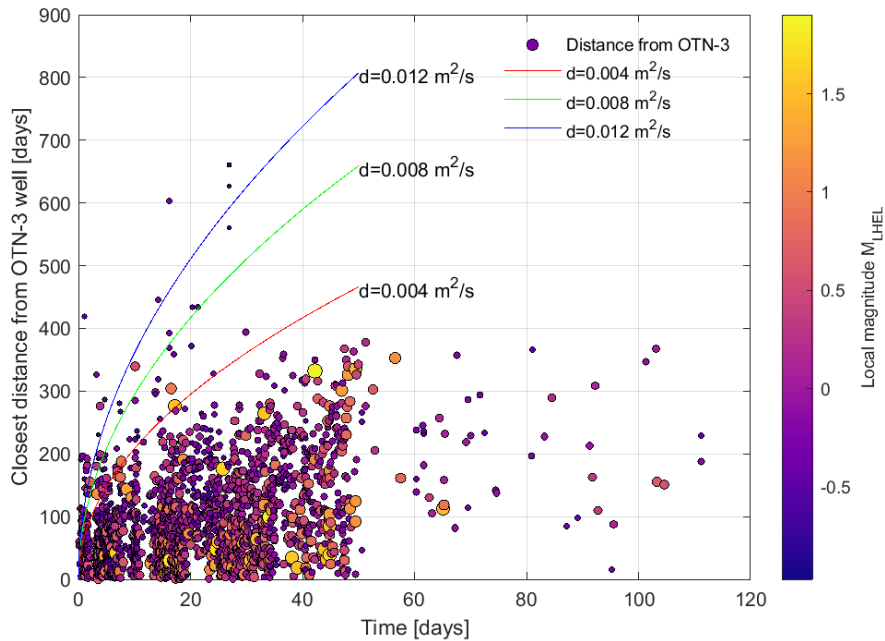
We shortened and restructured the entire section "Seismic catalog update" in the Results part to make it more unified with the Methodology part. A description of the seismic catalog and its reprocessing has now been moved to the data publication. We kept the discussion related to post-stimulation events, as these were not analyzed yet by Kwiatek et al. (2019) or by Hillers et al. (2020).

As mentioned in the response of comment #4 above, by using the updated catalog with a  $V_P/V_S$  ratio of 1.71, the hypocenters are now more symmetrically located around the borehole trace (Fig. 3b) and no longer below as it was the case using a  $V_P/V_S$  ratio of 1.67.

**13) Ln 364. It is interesting that the post-stimulation seismicity does not show any systematic migration. This observation should be supported by a sort of distance-time or coordinate-time plot. In fact, even the existing papers of Kwiatek and Hillers on the Helsinki stimulation do not show such data.**

Authors:

Thank you for this comment. We have produced a distance-time plot for the entire stimulation including all separate phases. For each event we took the shortest distance to the open-hole section of the injection well. For phases 1 and 2 we find relative fast migration to roughly 200 m to the well. Starting with phase 3 some events indicate migration out to 400 m distance to the well, but not further. This holds for the post-stimulation phase. The diagram is added to the data publication.



**14) Ln 381. To see the events at perimeter these should be shown on top of the others, e.g. in grey.**

Authors:

We updated Fig. S4 (in the revised manuscript S3) by plotting the events with  $M_w \geq 1$  which occurred during the stimulation in dark grey on top of all relocated events (light grey) to highlight the narrow zone. We further color-coded events with  $M_w \geq 1$  which occurred after the end of stimulation in orange to indicate that these events are located at the perimeters of the narrow zone.

We also added to the caption of this Figure the following sentence:

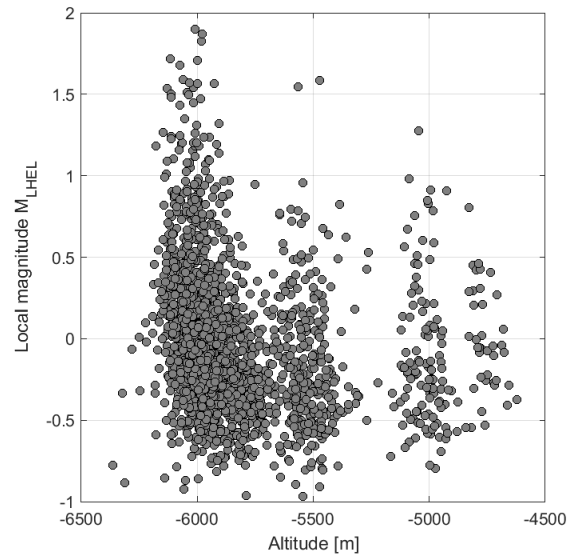
“Events with  $M_w \geq 1$  that occurred during and after the stimulation are color-coded as dark grey and orange, respectively.”

**15) Ln 393. Please argue for the highest expected pore pressure perturbation at the bottom of the permeable zone.**

Authors:

(see also reply to comment #16). The largest pore pressure perturbation is simply expected to be at or close to the well and will progressively decrease with increasing distance. Updated seismic catalog shifted events to shallower depths so they are not significantly deeper than the bottom-hole of injection well *OTN-3*. Thus, the highest seismicity activity and largest seismic events are not anymore at the “bottom of the permeable zone”, but are correlated to the bottom-hole of the injection well *OTN-3*. It is expected that this area is characterized by highest pore pressure perturbation, as this is where injection was performed in stages 1-3. Attached here is the figure from data publication showing relation between magnitude and depth.

We replaced “bottom” with “deepest” zone in the referred sentence, pointing out to the fact that largest events occur in the bottom cluster.



**16) Ln 400. The depthward migration is not visible in Fig. 3. And further, it is very unlikely that water would flow down in the expected lithostatic conditions of the rock formation where no open fractures are expected. On the contrary, water tends to flow up due to the buoyancy effect cause by the difference in density of water and rock.**

Authors:

We agree with the reviewer that such behavior is quite unexpected, although it is observed in some highly fractured reservoirs (see e.g. Kwiatek et al., 2015, Kwiatek et al., 2018). However, the updated seismic catalog with new  $V_P/V_S$  ratio effectively shifted all events to the shallower depths, rendering original comment on depth migration doubtful. It is still visible that in later stages the seismicity in the bottom cluster tends to locate at larger depths (see previous figure), but the depth of later events is not significantly exceeding the depth of bottom hole of *OTN-3*. This restrained us from suggesting that water flows down, and we suggest that occurrence of seismicity is simply related to pore pressure perturbation that is stronger around the bottom part of injection well *OTN-3*.

**17) Ln 442. In the Summary, the authors mention seismic catalog as a result of the study provided to the community. This sounds great, however I would welcome to see some quality analysis of the catalog, at least to show the Gutenberg-Richter distribution distinguishing the original catalog, the newly detected and newly located events.**

Authors:

We include the description of the seismic catalog and their properties to the data publication. Besides of providing details about the catalog reprocessing in the data publication, we include there statistical and spatio-temporal properties of developed catalog.

**18) Ln 449. The statement "The temporal behavior of the post-stimulation seismic moment release until bleed-off is still similar to the moment release observed during individual stimulation phases" sounds a bit vague.**

Authors:

We rewrote the sentence in the Summary and conclusions part:

*"Until shortly after the bleed-off, the increase in the cumulative moment release of the post-stimulation seismicity with time is comparable with the slope of the  $CM_0$  during individual stimulation phases but substantially less afterwards. This is especially observed for the seismicity of the deepest hypocenter cluster."*

**19) Ln 474-476. According to the unclear description of some parts I am not sure if all of the coauthors did really contribute to the manuscript (by e.g. the manuscript correction indicated in the Author contribution section).**

Authors:

We state the Author contribution as follows:

*"M.L.: data reduction, analysis and results interpretation, draft version of the manuscript, and associated data publication. G.K. and P.M.-G.: data analysis, results interpretation, and manuscript correction. M.B., G.D., and P.H.: results interpretation and manuscript correction. T.S.: project management, drilling and stimulation program development and managing, and manuscript correction."*

Comments of reviewer #1 to the Figures

**20) Fig S1. should be included as Fig. 1; this is much more informative than the present Fig. 1 which could be moved to Supplements.**

Authors:

We swapped Fig. S1 and Fig. 1.

**21) Fig. S2 overlaps with Fig. 2 and using different time scale (absolute vs. relative) makes it different to compare. Why not combining Fig.S2 and Fig.2 in a single plot?**

Authors:

Thank you for this suggestion, we combined both Figures to a new Fig. 2 using an absolute time scale. We therefore updated the following sentences in lines 237-239 in the manuscript:

*"The moment magnitudes of the absolute located and relocated seismicity is plotted with time during and after shut-in as grey and orange dots in Fig. 2. The five different stimulation phases (P1-P5) performed in 2018 are also shown in Fig. 2 in combination with the wellhead pressure and seismic event rate."*

**22) Fig. 2 is missing reference in the text. The caption does not explain the meaning of time - from which moment the days are counted? It is also not clear why you do not show also the time period during the stimulation as indicated in the manuscript title and also shown in Fig. 3.**

Authors:

Thank you for mentioning the missing reference of Fig. 2. With combining Fig. 2 and Fig. S2 to a new Fig. 2 in the revised manuscript, the reference for Fig. 2 is now mentioned in line 238. For the updated Fig. 2, absolute times (in days) are now used for a better understanding.

Initially we wanted to keep the focus on the post-stimulation seismicity in the original Fig. 2 because this is mainly the new data and not analyzed by Kwiatek et al. (2019) or Hillers et al. (2020) and therefore, the time period during stimulation was not shown. However, the suggestion of combining Fig. 2 and Fig. S2 is a good idea and thus the seismicity and time period during the stimulation is now also presented. For the updated Fig. 2, we rewrote the caption as followed:

*"Stimulation protocol with moment magnitudes of induced seismicity during stimulation phases P1-P5 and post-stimulation time period. The magnitudes of absolute located and relocated events are shown as grey and orange dots, respectively. The green solid line presents the wellhead pressure during the stimulation. The seismic event rate per day is shown by the solid blue line."*

**23) Fig. 3: The caption should be better specified; e.g. mentioning the name OTN3 of the borehole is missing and the legend does not explain the colored bands along the borehole trace. Are these the stimulated sections and should their color correspond (at the moment it does not) to the colors of hypocenters?**

Authors:

We specified the caption by adding the name of the injection well *OTN-3* and explaining the color bands along the borehole trace of *OTN-3*.

We apologize for the confusion about the colored bands along the borehole trace. Unfortunately, the colors along *OTN-3* were wrongly plotted in Fig. 3. We updated the colors which are now corresponding to the colors of the five stimulation stages.

For a better visibility, we also changed the color of the stimulation phase P5 hypocenters to a darker yellow.

**24) Fig. 4 and 5: the yellow line is hardly visible.**

Authors:

We changed the color to a darker yellow in both Figures.

**25) Fig. 5: The three CM0 plots could be better shown with common Y axis, which would spare space and make them more legible, also a single legend would then suffice.**

Authors:

Thank you for this suggestion. We updated the Figure using one common y-axis and one legend for all three subplots now.

**26) Fig. 9: The black stress component are not visible enough, consider using different color.**

Authors:

We now use white as color for the stress component marker symbols and the marker text.

We updated the sentence in the caption of Fig. 9:

*"White upward and downward pointing triangle represent maximum and minimum principal stress axes  $\sigma_1$  and  $\sigma_3$ , respectively."*

**27) Fig. 10: Please indicate in the caption that the stress ratio R 0.53 determined in the stress inversion is used. And shift the Px markers a bit to the right, these are very hardly visible now.**

Authors:

We added the following sentence to the caption of Fig. 10:

*"A stress ratio of  $R = 0.53$  was used for stress inversion."*

For a better visibility, we also shifted the text of the P1 and P2 markers a bit further outside of each marker symbol.

References not used in the manuscript

Cesca, S., Ali, S., and Dahm, T.: Seismicity monitoring by cluster analysis of moment tensors, *Geophysical Journal International*, 196, <https://doi.org/10.1093/gji/ggt492>, 2014.

Kwiatek, G., Martínez-Garzón, P., Plenkers, K., Leonhardt, M., Zang, A., Specht, S., Dresen, G., and Bohnhoff, M.: Insights into complex subdecimeter fracturing processes occurring during a water injection experiment at depth in Äspö Hard Rock Laboratory, Sweden, *Journal of Geophysical Research: Solid Earth*, <https://doi.org/10.1029/2017JB014715>, 2018.

**Response to reviewer #2 comments: se-2020-139-RC2**

General comments of reviewer #2

**Seismicity associated with the stimulation of an Enhanced Geothermal System in Finland is presented. A variety of analytical tools are used to extract as much information as possible. While I do not have expert knowledge of the tools, they seem to have been competently used and deliver plausible results.**

**While I am not personally involved in EGS studies, I found the paper interesting because it relates to work that my group is doing with regard to seismicity induced by mining and the flooding of worked-out mines, as well as shale gas development.**

**I failed to meet the review deadline, for which I apologise. I downloaded a copy of the Manuscript supplementary material when I reviewed the paper on 14 November. I hope that the supplements are of the same high standard, but I have not checked this.**

Authors:

We apologize for the problem of downloading the supplements and hope that the figures in the supplements also satisfy your expectations.

**Generally the paper is well-written. There are some minor grammatical errors that I have indicated on the attached annotated version of the manuscript. The referencing style is also inconsistent - some paper titles are in Sentence case, others in Title Case.**

Authors:

Thank you for indicating grammatical errors. We corrected all of them in the revised manuscript.

**There are also a few instances where I found the discussion difficult to follow or figures difficult to interpret. I have highlighted these and offered suggestions for improvement.**

Authors:

We address the comments and suggestions in detail below where each of them is listed and followed by our response.

Particular comments of reviewer #2

**1) Ln 225: ‘...Fig S2.’ I was not able to view the supplementary figures.**

Authors:

We again apologize for the problem.

**2) Ln 233-235: “Two events with  $M_w \geq 0.9$  occurred within the first 11 days of the post-stimulation phase. Two further  $M_w > 1$  events occurred within 24 hours and 17 days after the stimulation ended, one with moment magnitude of 1.6 (Fig. 2).”**

**I am confused. Perhaps I do not really understand what you mean by 'after shut-in' and 'end of injection, 'bleed-off of wellhead pressure', 'post-stimulation phase'. After enlarging the graph, I count the seven events, three occurring just after the dashed line (bleed-off). I then see 3 events  $\geq 0.9$  in days 5-10.**

Authors:

Thank you for the hint that there are actually 3 events with  $M_w \geq 0.9$  in days 5-10. We apologize for this mistake. Indeed, there are 3 events instead of only 2. We corrected the number in the manuscript.

**3) Ln 253-254: “...with two of them located on the NW flank of the injection well OTN-3...”**

**Figure 3a only shows one red rectangle to NW of OTN-3. Is the second cluster the events that fall mostly in the cell defined by easting (-600;-400); northing (-200; 0)?**

Authors:

Yes, with the second cluster located at the NW flank of the injection well OTN-3 we meant the clustered post-stimulation events that are located mostly in this cell.

**4) Ln 267-268: “The temporal evolution of the  $CM_0$  separated for each hypocenter cluster is shown in Fig. 5.”**

**Please make it absolutely clear to the reader where these three clusters lie. I suggest that you circle and label them in Figure 3.**

Authors:

We marked the three main hypocenter clusters by dashed rectangles in Fig. 3b and labeled them with the same names as we used in Fig. 5 to avoid any misunderstanding.

We further changed the following sentence in the manuscript (lines 281-282):

*"The temporal evolution of the  $CM_0$  separated for each hypocenter cluster, marked in Fig. 3b, is shown in Fig. 5."*

**5) Ln 325: "...due to appearing ambiguities in..."**

**I am not sure what you mean by 'appearing ambiguities'. Why not just 'amiguities'?**

Authors:

The word "appearing" does not really explain ambiguities any further in this context. We therefore deleted the word "appearing" in the manuscript to not confuse the readers.

**6) Ln: 401: "...gravity of the cool water..."**

**It not clear what you mean here. Perhaps 'gravity-driven movement of the cool water into ...'**

Authors:

Yes, the movement of the cool water into warm and less dense pore fluid would be driven by gravity. Thus, any further pressure would not be needed to migrate the water towards deeper parts of the reservoir. However, with obtaining new results (please see also responses to comments #15 and #16 of reviewer RC1), the statement is now more doubtful and thus, we deleted the sentence in the manuscript.

**7) Ln 434: "...lightened up..."**

**Not sure what you mean by 'lightened up'. Perhaps 'activated'.**

Authors:

Yes, with "lightened up" we mean "activated".

We changed the sentence in lines 452-453 as followed:

*"The 2018 seismicity activated a pre-existing network of small-scale parallel fractures dipping to ENE, in agreement with the dip direction of the inclined part of the injection well."*

**8) Ln 460: "...the gravitation-driven downwards migration..."**

**The physics behind the 'gravity-driven migration' is not clear to me. Is this related to the sinking of the cooler water?**

Authors:

The observation of the depthward migration of seismicity with time would be comparable e.g. with induced seismicity at The Geysers geothermal field (Kwiatek et al., 2015). For the Geysers, this depthward seismicity migration documents also a migration of cooler injected water into warmer pore fluid toward greater depth without any further pressure needed. The depthward migration of the water is also facilitated by steeply dipping faults which are well-known at The Geysers.

**9) Ln 463: "...but weak faults..."**

**Not sure what you mean by "but weak faults ..". Perhaps. These are thought to be weak faults ....**

Authors:

Yes, these fractures are thought to be weak faults.

We updated the sentence in the manuscript:

*"We conclude that seismic slip occurs on sub-parallel network of favorably oriented pre-existing but weak fractures, striking in NNW-SSE direction and dipping 45° ENE."*

**10) Ln 487-488: "...Seismic Moment Evolution During Hydraulic Stimulations,..". Sentence case, not Title Case.**

Authors:

Thank you for the hint. We changed the reference into sentence case.

**11) Ln 518-519: "Hardebeck, J. and Shearer, P.: A New Method for Determining First-Motion Focal Mechanisms, Bulletin of the Seismological Society of America, 92, 2264–2276, <https://doi.org/10.1785/0120010200>, 2002." I would expect the reference to follow Hardebeck and Michael.**

Authors:

Thank you for noticing this mistake. We swapped the reference of Hardebeck and Shearer (2002) with the reference of Hardebeck and Michael (2006).

Comments of reviewer #2 to the Figures

**12) Figure 3. I find the display confusing. The colours used to show the seismic events correlate well with the legend; however, the colours on the trace of the well do not.**

**When I enlarge the Figure 3b I see a bright red tip; above it is an olive green section; and above that a bright green section, then a blue section, and finally a purple section. Are these five sections meant to correlate with P1 - P5?**

**I also see several red circles plotted on the well trace between -5500 and -5650 (and one at -5500). What do these signify?**

Authors:

We apologize for the confusion about the colored bands along the borehole trace in Fig. 3. Unfortunately, the colors along OTN-3 were wrongly plotted. The colors should correlate with the colors of the five stimulation stages. Therefore, we updated the bands, now using the same colors as for P1-P5.

For a better visibility, we also changed the color of the stimulation phase P5 hypocenters to a darker yellow in Fig. 3.

We also apologize for the confusion about the small red circles. This was a mistake in plotting. In the updated version of Fig. 3, we excluded these circles.

**13) Figure 4. Figure 2 indicates that seismicity was recorded for 65 days after the end of injection. As I read it, this figure only shows the cumulative moments for 30 days. Am I reading it correctly? If so, please note this in the caption and text.**

Authors:

Yes, this is correct, Fig. 4 only presents the time period of 30 days for each stimulation phase and indeed, the post-stimulation time period was 63 days long. However, we decided to not plot the full 65 days due to an insignificant increase in the cumulative seismic moment after 30 days of the end of injection.

We changed the following sentence in the caption of Fig. 4:

*"For a time period of 30 days, the temporal evolution of cumulative seismic moment release for the relocated seismicity is shown for each injection phase as well as for the post-stimulation phase."*

We also changed the following sentence in the text (lines 274-276):

*"Here, we show the temporal evolution of the cumulative seismic moment ( $CM_0$ ) release for a time period of 30 days during the post-stimulation period and compare it with the evolution before shut-in of injection."*

**14) Figure 5. Please make it absolutely clear to the reader where these three clusters lie. I suggest that you circle and label them in Figure 3. Ensure that the time axis is marked so that it is clear to the reader that it covers the same duration as Figure 5 i.e. more than 10 days.**

Authors:

Thank you for the suggestion. To avoid any misunderstanding or confusion, we marked and labeled the three different clusters in the updated Fig. 3b, as already mentioned in the response of comment 4.

We also changed the x-axes in Fig. 5 to show and label the same time period as the x-axis in Fig. 4.

# Seismicity during and after stimulation of a 6.1 km deep Enhanced Geothermal System in Helsinki, Finland

Maria Leonhardt<sup>1</sup>, Grzegorz Kwiatek<sup>1</sup>, Patricia Martínez-Garzón<sup>1</sup>, Marco Bohnhoff<sup>1,2</sup>, Tero Saarno<sup>3</sup>, Pekka Heikkinen<sup>4</sup>, and Georg Dresen<sup>1,5</sup>

5 <sup>1</sup>Helmholtz Centre Potsdam, GFZ German Research Centre for Geosciences, Section 4.2: Geomechanics and Scientific Drilling, Potsdam, Germany, <sup>2</sup>Department of Earth Sciences, Free University of Berlin, Berlin, Germany, <sup>3</sup>St1 Deep Heat Oy, Helsinki, Finland, <sup>4</sup>Department of Geosciences and Geography, University of Helsinki, Helsinki, Finland, <sup>5</sup>Institute of Earth and Environmental Sciences, University of Potsdam, Potsdam, Germany

10 *Correspondence to:* Maria Leonhardt (maria.leonhardt@gfz-potsdam.de)

**Abstract.** In this study, we present a high-resolution dataset of seismicity framing the stimulation campaign of a 6.1 km deep Enhanced Geothermal System (EGS) in Helsinki suburban area and discuss the complexity of fracture network development. Within St1 Deep Heat project, 18,160 m<sup>3</sup> of water was injected over 49 days in summer 2018. The seismicity was monitored by a seismic network of near-surface borehole sensors framing the EGS site in combination with a multi-level geophone array located at  $\geq 2$  km depth. We expand the original catalog of Kwiatek et al. (2019) ~~including and provide the community with the dataset including~~ detected seismic events and earthquakes that occurred two month after the end of injection, ~~totalling~~ totaling to 61,163 events. We relocated events of the catalog with ~~sufficient number of available phase onsets and~~ moment magnitudes between  $M_w$  -0.57 and  $M_w$  1.9 using the double-difference technique and a new velocity model derived from a post-stimulation vertical seismic profiling campaign. The analysis of the fault network development at reservoir depth of 4.5-7 km is one primary focus of this study. To achieve this, we investigate 191 focal mechanisms of the induced seismicity using a cross-correlation based technique. Our results indicate that seismicity occurred in three spatially separated clusters centered around the injection well. We observe a spatio-temporal migration of the seismicity during the stimulation starting from the injection well in northwest (NW) - southeast (SE) direction and in northeast (NE) direction towards greater depth. The spatial evolution of the cumulative seismic moment, the distribution of events with  $M_w \geq 1$  and the fault plane orientations of focal mechanisms indicate an active network of at least three NW-SE to NNW-SSE orientated permeable zones which is interpreted to be responsible for migration of seismic activity away from the injection well. Fault plane solutions of the best-constrained focal mechanisms as well as results for the local stress field orientation indicate a reverse faulting regime and suggest that seismic slip occurred

30 on a sub-parallel network of pre-existing weak fractures favorably oriented with the stress field, striking NNW-  
SEE with a dip of 45° ENE, parallel to the injection well.

## 1 Introduction

Deep geothermal energy is considered as a potential source of low CO<sub>2</sub>-emission energy to replace fossil fuels. The successful development of deep geothermal reservoirs is crucial for the economic production of hot fluids for  
35 energy production. However, crystalline basement rocks hosting deep geothermal reservoirs in general are low-  
porosity and low-permeability formations. In Enhanced Geothermal Systems (EGS) hydraulic stimulation with  
massive fluid injection is applied to improve reservoir permeability (e.g. Giardini, 2009). Fluid injection at depth  
in EGS stimulations and in waste-water disposal is commonly associated with induced seismicity (e.g. Ellsworth,  
2013; Majer et al., 2012). Successful mitigation of induced seismic hazard is important for public acceptance of  
40 geothermal projects as significant concern exists related to the occurrence of larger induced earthquakes during  
previous EGS projects, e.g. in Basel and St. Gallen, Switzerland (e.g. Giardini, 2009; Diehl et al., 2017) or most  
recently in Pohang, South Korea (Hofmann et al., 2019; Ellsworth et al., 2019).

A well-designed seismic network is pre-requisite for high-resolution data acquisition, real-time seismic  
monitoring and analysis of induced seismicity (e.g. Bohnhoff et al., 2018). Subsequent feeding of seismic data into  
45 a traffic-light-system (TLS) may substantially contribute to mitigate the associated seismic hazard and risk. A  
successful and safe approach to stimulation of the world's deepest EGS in the metropolitan area of Helsinki was  
recently presented by Kwiatek et al. (2019). Over 49 days in summer 2018, the St1 Deep Heat Company injected  
more than 18,000 m<sup>3</sup> of water at 6.1 km depth. A  $M_w$  2.1 red alert threshold of the TLS defined by the local  
authorities was successfully avoided by a careful adjustment of the hydraulic energy input in response to real-time  
50 monitoring of the spatio-temporal evolution of seismicity. The largest seismic event was confined to a moment  
magnitude of  $M_w$  1.9 (Ader et al., 2019; Kwiatek et al., 2019).

High quality state-of-the art analysis of induced seismic waveform data is crucial for a detailed reservoir  
characterization (Kwiatek et al., 2013). High precision locations of hypocenters are typically obtained by applying  
relocation techniques such as the double-difference method (Waldhauser and Ellsworth, 2000). Using relocated  
55 data, a precise spatio-temporal evolution of induced seismicity can be tracked providing insight in fluid migration  
pathways in the reservoir (e.g. Kwiatek et al., 2015; Diehl et al., 2017). In addition, seismic source parameters  
such as seismic moment and source size provide crucial insights into the fracture network geometry.

Bentz et al. (2020) recently showed that many EGS fluid injections display an extended period of stable  
evolution of the cumulative seismic moment. Following Galis et al. (2015), this indicates the growth of self-

60 arrested ruptures, in contrast to unstable increase of seismic moment resulting in runaway ruptures that are only limited by the size of tectonic faults. Thus, unusual trends or potential changes in the seismic moment evolution may provide information on growth and activation of ruptures and thus also on the anthropogenic seismic hazard and subsequent risk. For example, Bentz et al. (2020) observed a steep and not stabilizing increase of the cumulative seismic moment potentially signifying unbound rupture propagation during stimulation for the Pohang  
65 EGS project. Dynamic source characteristics of seismic events including radiated energy, stress drop and apparent stress allow the evaluation of seismic injection efficiency (Maxwell, 2008) and the estimation of the energy budget of a stimulation campaign. Moreover, focal mechanisms provide important information for hazard assessment, as they can illuminate activation of large pre-existing structures such as major and potentially critically pre-stressed faults (e.g. Deichmann and Giardini, 2009; Ellsworth et al., 2019). Using focal mechanisms, Ellsworth  
70 et al. (2019) showed that induced seismicity activated a fault zone which ultimately triggered the large  $M_w$  5.5 earthquake at Pohang. The authors suggested that seismic analysis performed during stimulation sequences may provide early information on increasing seismic hazard. In addition, stress tensor inversion of focal mechanism data using e.g. the *MSATSI* (Martínez-Garzón et al., 2014) or *BRMT* (D'Auria and Massa, 2015) approaches allow the estimation of potential changes of the local stress field but require high-quality seismic waveform data from  
75 dense local seismic networks. Studying of the spatial and temporal variations of the stress field orientation contribute to understanding complex seismo-mechanical processes occurring in the reservoir during injection (Kwiatek et al., 2013). Martínez-Garzón et al. (2013) first observed a clear correlation of temporal stress changes in response to high injection rates at The Geysers geothermal field.

In this study we present a refined high-resolution dataset of seismicity induced during stimulation of the  
80 world's deepest geothermal EGS in the Helsinki suburban area in 2018 (Kwiatek et al., 2019; Ader et al., 2019; Hillers et al., 2020). The data was collected using a combined seismic network of individual sensors in shallow boreholes framing the injection site combined with a multi-level vertical geophone array at  $\geq 2$  km depth. Our dataset expands, refines and completes the original study of Kwiatek et al. (2019). We include seismic events which occurred after the end of the hydraulic stimulation and refine the seismic catalog using double-difference  
85 relocation with a new ~~derived~~-velocity model derived from a post-injection Vertical Seismic Profiling (VSP) campaign. To analyze the structural complexity of the reservoir, we investigate the spatio-temporal seismicity evolution and the temporal as well as spatial distribution of the seismic moment release during and after stimulation. This analysis is supported by an extensive catalog of source mechanisms derived from a cross-correlation based technique. Information on the local stress field orientation is derived from seismicity data. We  
90 discuss the evolution of potentially permeable zones in the reservoir and the re-activation of a network of small-scale fractures during and after stimulation.

## 2 Methodology

### 2.1 Seismic catalog reprocessing

Expanding the study of Kwiatek et al. (2019), we enhanced, reprocessed and relocated the original seismic catalog now also including post-injection events between July 22<sup>nd</sup> and September 24<sup>th</sup>. During and after the stimulation, induced seismicity was monitored by a dense seismic network of three-component sensors consisting of a 12-level vertical borehole array as well as 12 near-surface seismometers with full azimuthal coverage. The borehole array with 15 Hz sensors, sampled at 2 kHz, was installed at a depth from 1.95 to 2.37 km in the monitoring well *OTN-2* close to the injection well *OTN-3* whereas the 4.5 kHz near-surface seismometers, sampled at 500 Hz, were placed in wells with depths between 0.3 to 1.15 km and lateral distances of 0.6 to 8 km around the injection well (Fig. S1).

The reprocessed seismic catalog with description of its properties is available as separate data publication (see section *data availability*) and consists of 5,456 events that were detected and located during and after the stimulation (industrial monitoring) and reprocessed in our study. A total of 55,707 smaller events were further detected during and after the stimulation but were not located or processed later on. These were also included in published seismic catalog. For further explanation about the original seismic catalog see Kwiatek et al. (2019).

~~During the stimulation, the initial catalog used for evaluating the industrial success of the stimulation consisted of 6,150 events with a moment magnitude range of [ 1.47 1.9], located around the injection well *OTN-3* at an epicentral distance of less than 5 km and at depth of 0.5 to 10 km (Kwiatek et al., 2019). Events with  $M_w > 0.7$  were manually revised. The moment magnitudes were estimated from the industry catalog derived local magnitudes  $M_{HEL}$  by calculating the seismic moment  $M_0$  and using the formula of Hanks and Kanamori (1979) as described by Kwiatek et al. (2019). A total of 55,013 smaller events were further detected during and after the stimulation but were not located and thus not used for evaluating the stimulation success.~~

~~From the industrial catalog, we selected 3,464 events with at least 10 existing onset picks and depth between 4.5 and 7 km. For this study, we enhanced the sub-catalog by including 321 events that occurred after shut in of injection, i.e. after 22<sup>th</sup> of July 2018 at 15:52 UTC. These post injection events have also at least 10 onset picks and moment magnitudes between  $M_w = 0.5$  and  $M_w = 1.5$ . We manually revised 68 events of the post-stimulation seismicity with  $M_w > 0.07$  and refined the P and S wave onset picks if necessary.~~

### 2.1 Hypocenter locations

The enhanced sub-catalog of 5,456 events including 946 post-stimulation events was reprocessed applying a new updated 1D layered velocity model developed from P-wave onset times of calibration shots obtained during a post-

injection VSP campaign (Fig. [S1, see also data publication](#)). Due to a low Signal-to-Noise (S/N) ratio of the VSP data, the S-wave arrival times could not be determined. Thus, the  $V_p/V_s$  ratio was optimized by a trial-and-error procedure, where we ultimately constrained a  $V_p/V_s$  ratio of [1.714-67](#) that minimized the cumulative residual errors of all located events, and at the same time kept the first induced events [close to corresponding injection well OTN-3 in the direct vicinity of injection point \(cf. lowest injection interval in Fig. S1\)](#).

The hypocenter locations were estimated using the Equal Differential Time (EDT) method (Zhou, 1994; Font et al., 2004; Lomax, 2005) and the new VSP-derived velocity model. In addition, station corrections were applied. The minimization of travel time residuals:

$$130 \quad \left| \left| (T_j^{th} - T_i^{th}) - (T_j^{obs} - T_i^{obs}) \right| \right|_{L_2} = \min, \quad (1)$$

where  $T^{\text{th}}$  and  $T^{\text{obs}}$  are all unique pairs (i,j) of theoretical and observed travel times of P- and S-phases, were resolved using the Simplex algorithm (Nelder and Mead, 1965; Lagarias et al., 1998). [A total of 2,958 reprocessed events were located around the injection well OTN-3 at an epicentral distance of less than 5 km and at depth of 4.5 to 7 km. The hypocenters of these events were included to the reprocessed and published data catalog.](#)

135 To further refine the quality of hypocenter locations, [2,178 from the 2,958+93 absolute located events with of the absolute hypocenter sub-catalog with](#) at least 10 P-wave and 4 S-wave picks [as well as hypocenter depths between 4.5 and 7 km](#) were selected and the double-difference relocation technique (hypoDD) was applied using the new VSP-derived velocity model (Waldhauser and Ellsworth, 2000). An iterative least-square inversion was used to minimize residuals of observed and predicted travel time differences for event pairs calculated from  
140 the existing P- and S-wave picks of the selected catalog data. The residuals were minimized in ten iterations steps. For the last iteration, the maximum threshold for travel time residuals were set to 0.08 s and the maximum distance between the catalog linked event pairs was defined as 170 m. With the hypoDD method [1,986+984](#) events were relocated and thus [91+9](#) % of the selected [2,178+193](#) events. The residuals of the relocations have a root mean square error of 9 ms. The relocation uncertainties were then assessed using a bootstrap technique (Waldhauser and  
145 Ellsworth, 2000; Efron, 1982) leading to relative location precision not exceeding  $\pm 52$  m for 95 % of the catalog.

## **~~2.2 Spatial and temporal evolution of cumulative seismic moment~~**

~~We further analyzed the spatial and temporal evolution of the cumulative seismic moment based on the relocated seismic catalog. The cumulative seismic moment evolution with time was calculated for the entire catalog, and also separately for the three major spatial clusters. For the spatial distribution of the seismic moment, the area around the injection well was separated into horizontal bins of 50x50 m. The cumulative seismic moment of all events within each bin was then investigated by disregarding the depth.~~

150

### 2.32.2 Source mechanisms

To address the structural complexity of the reservoir in close proximity of the injection borehole below 4.5 km depth, source mechanisms were determined for a selected subset of events. For the 63 events with largest moment magnitudes located within the main (deepest) hypocenter cluster we first manually picked the P-wave onset polarities on the vertical component seismograms of all available stations. All waveforms were first filtered with a second order 120 Hz low-pass Butterworth filter. The same approach was applied to the 25 strongest events of the two shallower hypocenter clusters (see Fig. 3). The focal mechanisms (FMs) were determined using the *HASH* software (Hardebeck and Shearer, 2002). For each fault plane solution (FPS), associated uncertainties in a form of *acceptable* solutions are provided, calculated by perturbing take-off angles and azimuths by up to 3° (95 % confidence interval) to simulate the hypocenter location and velocity model uncertainties, respectively.

Aiming at increasing the catalog of focal mechanisms, we extended the focal mechanism calculations to smaller events with lower S/N ratio using the cross-correlation-based technique of Shelly et al. (2016). Additional 297 small events with lower S/N ratio were processed. To this end, the waveforms from a *template* set of 70 events with manually picked P-wave polarities were used to recover relative polarities of a *target* set of waveforms from 297 events, including 45 post-stimulation events and 18 events with manually-picked polarities. The waveforms of the events of both sets were first pre-processed focusing on the P-wave polarities obtained from the vertical components of all available stations. Seismograms were filtered with a second order 120 Hz low-pass Butterworth filter and a window length of 0.064 s including 0.012 s before the P-wave first motion. After a few trials, the low-pass Butterworth filter was fixed to 80 Hz for three stations of the satellite network due to a higher quality of the estimated polarity results for these stations. Considering the stations separately, each extracted waveform from the *target* set was cross-correlated with all remaining waveforms forming the *template* set. This resulted, for a particular station and *target* event, in a vector of 70 cross-correlation (CC) coefficients with the sign representing the relative polarities between *target* and *template* P-wave onsets for a particular station. Following Shelly et al. (2016), if the lag time of the largest cross-correlation peak was lower than 0.2 times the extracted wavelength, the CC was accepted and used as a relative polarity estimation between *target* event and *template*. The polarity estimates obtained from the CC values between the picked *template* and *target* events are relative and weighted by the absolute value of corresponding cross-correlation coefficient. Thus, the sign of the estimated polarity of the *target* event will be positive if the *template* and the *target* event have the same P-wave first motion.

180 For each station  $k$ , the vectors containing relative polarity estimates between one target event  $i$  and all templates  $j$  were gathered in a  $i$ -by- $j$  matrix.

~~To investigate the most reasonable estimated polarity pattern of each target event  $i$ , a~~ A Singular Value Decomposition (SVD) was applied to the relative estimated polarity matrix of each station  $k$  to extract the strongest ~~common~~ signal of any *target* event obtained by the first left singular vector of the SVD (Shelly et al., 2016; Rubinstein and Ellsworth, 2010). The estimated first left singular vectors for each station  $k$  are gathered in a  $i$ -by- $k$  matrix

$$PP_{ik} = \begin{bmatrix} pp_{i1} & \cdots & pp_{ik} \\ \vdots & \cdots & \vdots \\ pp_{i1} & \cdots & pp_{ik} \end{bmatrix}, \quad (2)$$

which then represents the most reasonable, however, still relative polarity pattern of each *target* event.

To reduce the polarity ambiguity of the events, we considered 18 events with known manually picked polarities included in the *target* event set. ~~For each station  $k$ , t~~The SVD-derived polarities of these events were compared with manually picked polarities to investigate whether the polarities have similar or opposite signs. ~~In case of same polarities, the SVD-derived polarities of other events should also show the right sign for the particular stations.~~

Estimated polarity patterns of the events were then used to calculate focal mechanisms. For further investigation we only considered events with a good quality of estimated focal mechanisms no matter if the polarities were manually picked or estimated. Thus, we only used events with focal mechanisms that have root mean square fault plane uncertainties less or equal  $35^\circ$  (Hardebeck and Shearer, 2002). The final catalog of focal mechanisms includes ~~s~~ 191 events with either manually or estimated polarity pattern ~~and is presented with associated uncertainties in the data publication (see section data availability).~~ ~~The focal mechanisms generally show reverse faulting motions with NNW-SSE striking fault planes.~~

### 200 ~~2.3~~ **2.4 Complexity of source mechanisms**

To investigate the variability of the estimated focal mechanisms, we first calculated the principal axis directions of the double-couple seismic moment tensor derived from focal mechanism for each event. To quantify the level of similarity of any two focal mechanisms, we calculated the 3D Kagan rotation angle between principal axis directions of both events (Kagan, 1991; Kagan, 2007; Tape and Tape, 2012). Low values of Kagan angle ( $<20^\circ$ ) suggest that focal mechanisms of two events are similar. To further group events into families with similar source mechanisms, an unsupervised classification of the 191 events was performed using a hierarchical cluster analysis based on the similarity of estimated Kagan rotation angles. Thus, the measurement of proximity  $PR$  of any two focal mechanisms was defined as a distance metric

$$PR_{ij} = \frac{1 - \cos(\theta_{ij}^{rot})}{1.5}, \quad (3)$$

210 where  $\theta_{ij}^{rot}$  is a matrix containing the estimated rotation angles between any focal mechanism pair  $ij$ . In the following, the dendrogram tree based on the hierarchical clustering was used to separate focal mechanisms into different families.

To investigate the local stress field orientation in the reservoir surrounding the injection well, we applied the linear stress inversion method *MSATSI* (Martínez-Garzón et al., 2014) and the Bayesian-analysis-based and  
215 nonlinear stress inversion method *BRTM* of D’Auria and Massa (2015). In both methods, the strike, dip and rake angles of the fault plane solutions from the focal mechanisms were used to invert for the orientation of three stress axes. A relative measure of the stress magnitude is obtained by the stress shape ratio  $R$  (e.g. Hardebeck and Michael, 2006; Lund and Townend, 2007)

$$R = \frac{\sigma_1 - \sigma_2}{\sigma_1 - \sigma_3}. \quad (4)$$

## 220 3 Results

### ~~3.1 VSP-derived velocity model~~

~~The 1D VSP derived velocity model shows a velocity inversion between 3 and 6 km depth (Fig. 1). The maximum P wave velocity is  $0.15 \text{ km s}^{-1}$  larger than the maximum velocity modelled by Kwiatek et al. (2019) where a constant velocity of  $6.4 \text{ km s}^{-1}$  starting at 3 km depth was assumed. Below the velocity inversion, a constant  
225 velocity of  $6 \text{ km s}^{-1}$  is suggested from sonic logs which were used for velocity estimation between 5.1 km and 6.4 km depth. We assumed  $V_p/V_s = 1.67$  considering the mean cost function uncertainties of the absolute hypocenter locations for different  $V_p/V_s$  ratios as well as the spatial distribution of the initial events around the open hole of the injection well. This is slightly lower than the  $V_p/V_s$  ratio of 1.68 used for the velocity model presented in Kwiatek et al. (2019).~~

### 230 3.23.1 Seismic catalog update

~~We extended the original seismic catalog analyzed in Kwiatek et al. (2019) by 321 events that occurred after the stimulation campaign. In total 3,785 events were located in absolute sense using the new VSP derived velocity model and refined P and S wave picks. We further relocated 1,981 events with at least 10 P and 4 S wave picks applying the double difference relocation method. The expanded event catalog together with the event detection  
235 is available as data publication (see section *data availability*).~~

~~The selected sub-catalog used for absolute hypocenter locations consists of 3,785 events with magnitudes between  $M_w = 0.8$  and  $M_w = 1.9$ . The moment magnitudes of the absolute located and relocated seismicity is plotted with time~~

during and after shut-in ~~as grey and orange dots~~ in Fig. S2. The five different stimulation phases (P1-P5) performed in 2018 are also shown in Fig. S2 in combination with the wellhead pressure ~~and seismic event rate~~. Further details of the stimulation protocol and seismicity evolution are presented by Kwiatek et al. (2019), and here we focus on analysis of post-stimulation seismicity.

The ~~213321~~ post-injection events ~~with absolute locations~~ were detected during a time period of two months after shut-in of injection and ~~all had displayed~~ magnitudes  $M_w \geq -0.75$ . After shut-in, the seismic event rate ~~increased shortly and~~ started to rapidly decrease ~~after bleed-off of the well~~ (Fig. 2). This decrease in activity continued until the 5<sup>th</sup> day after the end of the injection followed by a slower decrease thereafter. During the first two days after shut-in, seven events with  $M_w \geq 1.0$  occurred. The largest event had a magnitude of  $M_w = 1.5$  and occurred directly after bleed-off, followed closely by two  $M_w 1.3$  events. ~~ThreeTwo~~ events with  $M_w \geq 0.9$  occurred within the first 11 days of the post-stimulation phase. Two further  $M_w > 1$  events occurred within 24 hours and 17 days after the stimulation ended, one with moment magnitude of 1.6 (Fig. 2). The latter events coincided with engineering operations performed in the injection well.

The updated relocated hypocenters ~~of 1,981 events with at least 10 P wave and 4 S wave picks and magnitudes between  $M_w -0.7$  and  $M_w 1.9$~~  occurred in three spatially separated clusters elongated in southeast (SE) - northwest (NW) direction and centered along the injection well, in good agreement with Kwiatek et al. (2019) (Fig. 3). Elongation of the clusters in SE-NW direction is sub-parallel to the local maximum horizontal stress  $S_H^{\max} = 110^\circ$  (Kwiatek et al., 2019; Heidbach et al., 2016; Kakkuri and Chen, 1992). The main seismicity cluster centers around the open-hole section of the borehole ~~and. The uppermost hypocenter cluster is spatially separated into one main cloud and a second smaller cloud (Fig. 3b). The events within the smaller cloud mainly occurred during the two last stimulation phases (P4 P5) and thus, the separation is also recognizable in time domain. The main cloud of the uppermost cluster spans about 300 m in depth separated 100 m from a smaller cloud with 150 m vertical extend. The deepest hypocenter cluster spans 700 m depth (Fig. 3b).~~ This exceeds vertical relocation precision, which is well constrained due to sensors located in a vertical borehole. The spatio-temporal seismicity evolution during the stimulation developed in two preferential directions starting from the injection well: in NW-SE direction sub-parallel to the direction of  $S_H^{\max}$  as well as in northeast (NE) direction with depth.

~~68 post stimulation events with at least 10 P and 4 S wave onset picks could be relocated using the double difference technique and are shown as grey dots in Fig. 3.~~ The ~~relocated~~ post-stimulation events are mainly located at the outer edges of the clusters following the trend observed during the stimulation. The post-injection seismicity shows no spatial migration and seems to be mostly confined to three isolated clusters, with two of them located on the NW flank of the injection well OTN-3 (Fig. 3a). The largest post-stimulation events with magnitudes between  $M_w 1.0$  and  $M_w 1.5$  occurred at the NNW and SSE outer edge of the main cluster. These events are located

270 in close proximity to some of the largest events of the last stimulation phase P5 (red rectangles in Fig. 3a), when high seismicity rates were observed.

### 3.33.2 Temporal evolution of cumulative seismic moment

For the stimulation period, the temporal evolution of the cumulative seismic moment release is discussed by Kwiatek et al. (2019). Here, we show the temporal evolution of the cumulative seismic moment ( $CM_0$ ) release for a time period of 30 days during the post-stimulation period and compare it with the evolution before shut-in of injection. During the first two days of the post-stimulation period, the increase of  $CM_0$  was similar to the first two days of stimulation phases P1-P5 (Fig. 4). Shortly after bleed-off, the  $CM_0$  rapidly increased due to the three  $M_w \geq 1$  events (Fig. 2). Thereafter, the increase of post-stimulation moment release was substantially less compared to a similar time period during P1-P5. Only two single events occurred with  $M_w \geq 1$  during day 17, 280 seemingly triggered by post-stimulation engineering operations in the well.

The temporal evolution of the  $CM_0$  separated for each hypocenter cluster, marked in Fig. 3b, is shown in Fig. 5. For the upper cluster, the increase in the  $CM_0$  is visibly larger for the stimulation phase P1 than for the other phases. For stimulation phase P2, a substantial increase in  $CM_0$  occurred between day 4 and 5. For the central hypocenter cluster, a substantial increase in the  $CM_0$  is visible for stimulation phase P2, P4 and P5 at the beginning 285 of day 3 and also for P1 and P4 during day 6. For both upper and central clusters, the post-stimulation  $CM_0$  is substantially smaller compared to that from injection (Fig. 5a-b). The  $CM_0$  during post-stimulation in bottom cluster is similar to P2-P5 within the first two days and afterwards lower than P2-P5 for the main cluster. Inevitably, the bottom cluster that hosts the majority of the seismic activity also displays the highest  $CM_0$  (Fig. S23). We note that the slopes of the  $CM_0$  evolution are similar for the upper and central cluster, but steeper for the bottom cluster 290 (Fig. S23).

### 3.34 Spatial evolution of cumulative seismic moment

For the spatial distribution of the seismic moment, the area around the injection well was separated into horizontal bins of 50x50 m. The cumulative seismic moment of all events within each bin was then investigated by disregarding the depth. During stimulation, the largest moment release and level of seismic activity occurred at 295 the center of the main event cluster at the bottom of the injection well close to the open-hole section (Fig. 6a-b). Furthermore, larger events in the main cluster tend to locate at the greatest depths. Interestingly, a NNW-SSE alignment of enhanced cumulative seismic moment release is visible in the main hypocenter cluster in agreement with the preferred NW-SE trending direction of the two upper hypocenter clusters. The hypocenters of larger

events show a similar alignment (Fig. 6a, S34). A smaller area at the NNW outer flank of the bottom hypocenter cluster displays anomalously high  $CM_0$  release caused by large events occurring during the last injection phases and after injection (red rectangle in Fig. 6a-b). Interestingly, epicenters of two tectonic seismic events with  $M_W$  1.4 and  $M_W$  1.7 were reported to occur in 2013 a few kilometers NW of the bottom hole section of well *OTN-3* (Kwiatek et al., 2019).

### 3.45 Complexity of source mechanisms

We determined 191 single-event focal mechanisms (Fig. 7). Using the dendrogram tree based on hierarchical clustering (Fig. S45), events were separated into three distinct families (I-III) with similar focal mechanism orientations containing 99, 60 and 27 events, respectively (different coloring of beach balls in Fig. 7). Five events were not grouped in any of the three families and thus, were not considered any further. Events belonging to the three families are not separated spatially. Oblique reverse faulting is the dominant source mechanism type, which is in contrast to the regional strike slip regime (Kwiatek et al., 2019). The two largest events with reverse faulting were classified into family III. Fault plane solutions from all families indicate a range of preferred SSE-NNW to SW-NE strike directions, sharing comparable dips ranging approx. 35-50° (Fig. 7a and 7e). The source mechanisms of only a few events indicate strike-slip faulting, with two of them occurring after shut-in. A total of 14 estimated focal mechanisms are post-stimulation events (Fig. 7b, 7d and 7f). The post-stimulation events contained in the main hypocenter cluster at the bottom of the well have similar focal mechanisms as events during the stimulation. In the central hypocenter cluster, two strike-slip events occurred close by.

To further explore separation of the focal mechanisms into distinct families, we analyzed the rotation angle between principal P- and T-axes as a measure of mechanism (dis)similarity. We first calculated mean fault plane solution for each family. The strike/dip/rake-values of the mean fault plane solutions (FPS) for family I, II and III are 332°/47°/43° and 32°/51°/141° and 67°/36°/122°, respectively. The focal mechanisms with mean fault plane solutions and all best FPSs of each family are plotted in Fig. 8a-c. Hillers et al. (2020) recently estimated focal mechanisms for the 14 largest events for which the majority is similar to family I FMs. The calculated rotation angles between mean solutions of family I and II, I and III, II and III are 71°, 59° and 53°, respectively. Taking into account that focal mechanisms are assumed to be similar if the Kagan rotation angle is less than 20°, none of the three families is similar to each other. Difference between family I and II is the most prominent, whereas rotations I-III and II-III are comparable. However, despite mean solutions of different families are quantitatively distinct, the individual mechanisms are not necessarily very different (Fig. 8d-f) in between families. The total P-axis uncertainties are strongly overlapping between three families. At the same time, the T-axes uncertainties form three distributions that, while compared between families, are only partially overlapping. This

330 overall suggest that the FPSs may be sensitive to changes in polarities on individual stations located close to the nodal plane.

In the following, we analyzed qualitatively the polarity patterns of events forming three families. The most repetitive polarity pattern observed at each station for a particular family is plotted in Fig. 8a-c. We first verified consistency of polarity patterns for events with manually picked polarities (N=37/15/15 FPSs for family 335 I, II, III, respectively). We noted the strike slip mechanisms are attributed to least well-constrained focal mechanisms belonging to family II. The main substantial difference in the polarity patterns across families seems to be related to polarities observed at two stations *MALM* and *MUNK* (Fig. 8a-c). For family I, the polarities on these two stations are positive and extremely consistent among events forming the family (35 out of 37 events display such a behavior). For family II, we observe *MALM* and *MUNK* to have mostly negative and positive 340 polarity pattern, respectively. For family III, the situation is reversed with *MALM* and *MUNK* having predominantly positive and negative polarity pattern, respectively. We further analyzed qualitatively the polarity pattern of events with polarities estimated from cross-correlation based technique of Shelly et al. (2016). Here, the situation generally further complicates due to ~~appearing~~ ambiguities in resolving the polarities due to decreased signal-to-noise ratio. However, for the majority of the events forming family I, the resolved focal mechanisms still 345 show a consistent polarity pattern to that from manually picked ones, with only incidentally changing polarities on stations *UNIV* and *RUSK* located away and thus displaying lower signal-to-noise ratio. The pattern of resolved polarities for family II is generally comparable to that resolved for manual polarities. However, 19 out of 45 events have negative estimated polarities for *MALM* and *MUNK*, thus the resolved polarity patterns seem to vary more in comparison to that of family I. The events with estimated polarities for family III have the same patterns for stations 350 *MALM* and *MUNK* as the manually picked events except of one event. However, other stations with lower signal-to-noise ratio display sometimes varying resolved polarities. We suppose that 1) the attribution of focal mechanism to a particular family is substantially ~~dependent~~ depending on the polarity pattern of a limited number of stations that are ~~located~~being close to the nodal planes, and 2) family I focal mechanisms seem the most stable.

Using the *BRTM* and *MSATSI* stress tensor inversion methods based on 191 focal mechanisms, we 355 estimated the local stress field orientation. The variability of FMs to constrain the stress field inversion is given due to high Kagan rotation angles between the mean FPSs of the three families with  $53^\circ$  to  $71^\circ$ . The *BRTM* results show that the maximum principal stress axis  $\sigma_1$  is oriented almost horizontally with a trend of  $279^\circ$  and a plunge of  $4^\circ$  (Fig. 9). The minimum principal stress axis  $\sigma_3$  has a trend and plunge of  $185^\circ$  and  $67^\circ$ , respectively. The stress shape ratio is calculated with  $R = 0.53$ . The estimated orientation of  $\sigma_1$  deviates  $\sim 10^\circ$  from the local 360 maximum horizontal stress  $S_H^{\max}$  (Kwiatek et al., 2019). Using the *MSATSI* method, the trend and plunge of  $\sigma_1$  is

calculated with  $271^\circ$  and  $11^\circ$ , respectively. Thus, the estimated trend of  $\sigma_1$  deviates  $\sim 20^\circ$  from the maximum horizontal stress  $S_H^{\max}$ . The minimum principal stress axis  $\sigma_3$  is oriented with a trend of  $76^\circ$  and a plunge of  $79^\circ$ . The stress shape ratio is with  $R = 0.72$  larger compared with the *BRTM* estimate.

365 The stress inversion of the induced seismic events represents a local reverse faulting regime. This is in contrast to the regional strike-slip regime estimated from regional stress and borehole data (Kwiatek et al., 2019). Only the focal mechanisms of a few events present a dominant strike-slip faulting, which typically are smaller events with a less well constrained polarity pattern.

#### 4 Discussion

370 Analysis of the seismic data suggests that fluid injection was performed into a complex network of small-scale pre-existing and distributed fractures and minor faults, rather than activating a single, major fault (Kwiatek et al., 2019). In an effort to characterize the structural complexity of the reservoir in detail, we compiled a high-resolution dataset of hypocenters and single-event focal mechanisms by enhancing and refining the original seismic catalog.

375 The relocated events of our updated catalog show three separated spatial hypocenter clusters along the injection well in good agreement with Kwiatek et al. (2019) and Hillers et al. (2020). Hillers et al. (2020) used seismic data collected from an independent surface-based seismic network of dense sub-arrays, whereas Kwiatek et al. (2019) used the same seismic network as we do but a simplified velocity model and slightly different  $V_P/V_S$  ratio. The hypocentral depths of the events vary slightly between this and previous studies. We found that differences between absolute locations among these catalogs are likely explained by variations in  $V_P/V_S$  ratios and velocity models.

380 We also provide the first analysis of post-stimulation events expanding the seismic catalog to investigate potential changes in the seismicity pattern from stimulation to the post-stimulation period. Compared to the seismicity occurring during the stimulation, the post-stimulation seismicity shows no spatio-temporal migration and remains largely confined to three separate clusters. One cluster arose after bleed-off and is located at the NW flank of the central hypocenter cluster that formed during stimulation. The largest post-stimulation events occurred 385 at the NNW and SSE outer edges of the main hypocenter cluster where also anomalously higher seismicity rate and larger events were observed during the last stimulation phase P5 (cf. Fig. 3). For the main hypocenter cluster, the temporal evolution of the post-stimulation  $CM_0$  shows similarities to the injection period until bleed-off of the well with only small changes thereafter. This suggests that seismicity is driven by the elevated pressure in the reservoir due to the previous hydraulic pumping (=increased stored elastic energy). However, hypocenter

390 propagation requires active pumping. This is indicated by a much smaller residual increase in  $CM_0$  and no further migration of the seismicity after bleed-off and decrease in reservoir fluid pressure.

The spatio-temporal seismicity evolution during stimulation as well as the spatial distribution of the cumulative seismic moment release indicate clear alignment of the events in NW-SE direction in the two shallower hypocenter clusters which could signify activation of permeable zones along faults or joints oriented in this direction. Existence of these zones is supported by the results of *OTN-3* well logging, where intervals of highly damaged rocks were detected that roughly coincide with the intersection of the upper seismicity clusters and the well path. For the largest bottom seismicity cluster, the relocated seismicity is distributed diffusively around the injection well. However, larger seismic events form a distinct alignment along a NNW-SSE direction (Fig. 6a, S34) with post-stimulation events clearly located at the perimeter of the narrow zone (Fig. S34). This alignment indicates activation of another permeable zone similar to the two upper ones. The NNW-SSE trending orientation is coinciding with an abundance of very similar focal mechanisms from the best constrained family I events with strike direction nearly identical to the NNW-SSE alignment of hypocenters. Moreover, two natural micro-earthquakes with  $M_w$  1.7 and  $M_w$  1.4 occurred in 2013 a few kilometers NNW from the well (Kwiatek et al., 2019). Although there is no detailed information available on their depths due to limited coverage of the seismic network at their origin time, their epicentral location coincides with the NNW perimeter of the bottom NNW-SSE alignment hosting large induced seismicity events as well. These observations suggest that the stimulation activated at least three prominent NW-SE to NNW-SSE oriented permeable zones of subparallel fractures or faults that are responsible for seismicity migration away from the injection well during the stimulation. The deepest NNW-SSE trending zone is buried in a more disperse seismic activity forming the bottom cluster and hosts the largest induced (and likely earlier some natural) earthquakes. The fact that the largest events occurred in the ~~bottom-deepest~~ permeable zone may be simply related to the highest expected pore pressure perturbation in this volume due to injection and migration of fluids. Kwiatek et al. (2019) speculated that the maximum event magnitude is either limited by available fault sizes or strength of the faults. The total length of NNW-SSE trending permeable bottom zone (~650 m, Fig. S34), clearly marked by the numerous and very similar focal mechanisms, is much larger than the average size of a single  $M_w$  2 earthquake (~80 m diameter) with even lower relocation precision. We therefore suggest that the upper limit to maximum magnitude is related to the low fault strength.

For the main hypocenter cluster, the seismicity migrates ~~progressively beyond the injection intervals~~ towards the NE and towards greater depths, dipping in the same direction as the inclined portion of *OTN-3* well (Fig. 3). ~~The depth propagation of the seismicity may be affected by gravity of the cool water into warm and less dense pore fluid of the reservoir as e.g. observed at The Geysers geothermal field (Kwiatek et al., 2015).~~ The downward-propagation of seismicity may signify activation of small-scale fractures striking NNW-SSE and

dipping along the injection well. This is again supported by the catalog of source mechanisms forming family I events (cf. Fig. 7 and 8a). To further understand this striking observational and qualitative agreement of family I fault planes with spatial distribution and evolution of seismic activity, we tested which family of focal mechanisms is better oriented for failure within the local stress field. A projection of estimated FPSs in a Mohr circle diagram reveals fault plane orientation with respect to the stress field (Fig. 10). Optimally oriented fault planes are more likely to be activated (e.g. Vavryčuk, 2011), especially for weak faults. To calculate the failure criterion, we assumed a friction coefficient of  $\mu = 0.7$  as a mean value for faults in the Earth's crust (Vavryčuk, 2011). While projecting the selected one of the two nodal planes from each fault plane solution, we used the nodal plane that displayed higher instability coefficient  $I$  (cf. Vavryčuk, 2014; Martínez-Garzón et al., 2016):

$$I = \frac{\tau + \mu(\sigma_n + 1)}{\mu + \sqrt{1 + \mu^2}}, \quad (5)$$

with  $\tau$  and  $\sigma_n$  as the normalized shear and normal tractions, respectively and  $\mu$  as the friction coefficient.

Clearly, FPSs from family I are the most favorably oriented with respect to the local stress field (blue points and triangles in Fig. 10), as also indicated by the highest fault instability coefficients (Fig. S56). It turned out that the most optimally oriented fault plane is always the one trending NNW-SSE and dipping approximately in the direction of inclined portion of *OTN-3* well (indicated by P1 nodal planes in Fig. 8a). This is also confirmed by the mean solution of family I ( $332^\circ/47^\circ$  plane, blue P1 marker in Fig. 10) displaying the highest instability (Tab. S1). However, also the fault planes represented by the auxiliary plane of the mean solution of family I are quite favorably oriented (blue P2 marker in Fig. 10). Some of the family III events are also quite favorably oriented with the stress field. We note that instabilities of auxiliary planes of mean FPSs for family I and III are similar (green and blue P2 dots in Fig. 10, Tab. S1), in agreement with their mean auxiliary nodal plane orientations of  $210^\circ/60^\circ$  (P2 in Fig. 8b-c). Qualitatively, nodal planes from family II seem to be mostly unfavorably oriented with the stress field (orange points and triangles in Fig. 10), as indicated by the lowest instability coefficients (Fig. S56). However, some P1 nodal planes are striking N-S (cf. Fig. 8b) and thus showing quite similar orientations as the P1 FPSs of family I (Fig. 8a), leading to higher instability coefficients for these planes (orange dots and triangles close to blue and green P2 marker in Fig. 10). Here, we found 19 events of family II show in fact similar polarity patterns than that observed for family I events with only an opposite polarity for station *MUNK*.

The performed analysis of fault instability clearly showed that high-quality focal mechanisms constituting family I events display comparable oblique reverse component and optimally oriented fault planes striking approximately NNW-SSE and dipping around  $45^\circ$ . These fault plane orientations are in agreement with the estimated stress field, and they explain well the spatio-temporal evolution of seismicity with corresponding fluid migration pattern. The 2018 seismicity ~~activated activity lightened up~~ a pre-existing network of small-scale parallel

fractures dipping to ENE, in agreement with the dip direction of the inclined part of the injection well. Fault planes striking NNE-SSW to NE-SW and dipping around 60° were also indicated to be quite favorably oriented with the stress field represented by the auxiliary plane of the mean FPSs for family I and III. Drill bit seismic data suggest the existence of a steeply dipping NE-SW striking structure which might be activated by the 2018 seismic activity. We note the FM results are in good agreement with a limited number of 14 focal mechanisms of the strongest events presented in Hillers et al. (2020), which were all but one displaying reverse faulting motions.

## 5 Summary and conclusions

We present a new seismic catalog for the geothermal stimulation in Helsinki 2018 determining new locations and relocations on the basis of the new VSP-based velocity model and include the post-stimulation seismicity resulting in a catalog with 5,4563,785 events. The catalog is extended by the list of detections, accounting to 61,163 events provided to scientific community (see section data availability). The magnitude of completeness of the entire catalog is  $M_C = -1.10$ . The catalog is supplemented by 191 focal mechanisms calculated using polarity-based and cross-correlation based methods and is used to discuss the structural complexity of the reservoir.

Spatial migration of the seismicity is driven by enhanced pore fluid pressure due to active injection, as no spatial migration of the post-stimulation seismicity after bleed-off is found. ~~The temporal behavior of the post-stimulation seismic moment release until bleed-off is still similar to the moment release observed during individual stimulation phases. Until shortly after the bleed-off, the increase in the cumulative moment release of the post-stimulation seismicity with time is comparable with the slope of the  $CM_0$  during individual stimulation phases but substantially less afterwards. This is especially observed for the seismicity of the deepest hypocenter cluster.~~

An activated network of at least three NW-SE to NNW-SSE oriented fracture zones of up to 200 m thickness seems to be responsible for the significant seismic activity migration towards NW-NNW and SE-SSE away from the injection well. The deepest fracture zone also hosts much of the larger seismic events with magnitudes exceeding  $M_W \geq 1$ , suggesting elevated fluid volume and pore fluid pressure, leading to accumulation of hydraulic energy in this area, relaxed in larger seismic events.

Best-constrained focal mechanisms strike NNW-SSE in agreement with orientation of three fracture zones. Most of these mechanisms display ~45° ENE dipping oblique-thrust fault planes that were found to be critically stressed in the resolved local stress field. These fault kinematics explains well NNW-SSE migration of seismicity along damage zones, as well as the ~~gravitation-driven~~ downwards migration of ~~smaller~~ events towards NE-NNE, along the dip direction vector of the inclined portion on injection well.

We conclude that seismic slip occurs on sub-parallel network of favorably oriented pre-existing but weak fractures, ~~but weak faults~~ striking in NNW-SSE direction and dipping 45° ENE. The localization of seismic moment release in NNW-SSE trending zones suggest the existence of NNW-SSE trending damage structures or lithological differences that increase the mobility of fluids in this confined parts of the reservoir.

### **Data availability**

The seismic event catalog ~~will be with associated description of its basic statistical and spatio-temporal properties~~ is available through GFZ data services: <http://dataservices.gfz-potsdam.de/portal/> as a separate data publication. For the event detections, the catalog contains origin times, local and moment magnitudes. For located events, the catalog contains origin times, local as well as moment magnitudes, absolute locations in local Cartesian coordinate system and for relocated events also the double-difference relocated locations in local Cartesian coordinate system. The fault plane solutions (strike, dip and rake) with associated uncertainties of estimated focal mechanisms are also included in the data catalog.

### **Competing interests**

The authors declare that they have no competing interests.

### **Author contribution**

M.L.: data reduction, analysis and results interpretation, ~~and~~ draft version of the manuscript, and associated data publication. G.K. and P.M.-G.: data analysis, results interpretation, and manuscript correction. M.B., G.D., and P.H.: results interpretation and manuscript correction. T.S.: project management, drilling and stimulation program development and managing, and manuscript correction.

### **Acknowledgments**

We thank Ilmo Kukkonen and Peter Malin for the valuable discussions. G. K. acknowledges funding from DFG (German Science Foundation), Grant KW84/4-1. P. M.-G. acknowledges funding from the Helmholtz Association through the Helmholtz Young Investigators Group “Seismic and Aseismic Deformation in the brittle crust: implications for Anthropogenic and Natural hazard” (<http://www.saidan.org>).

## References

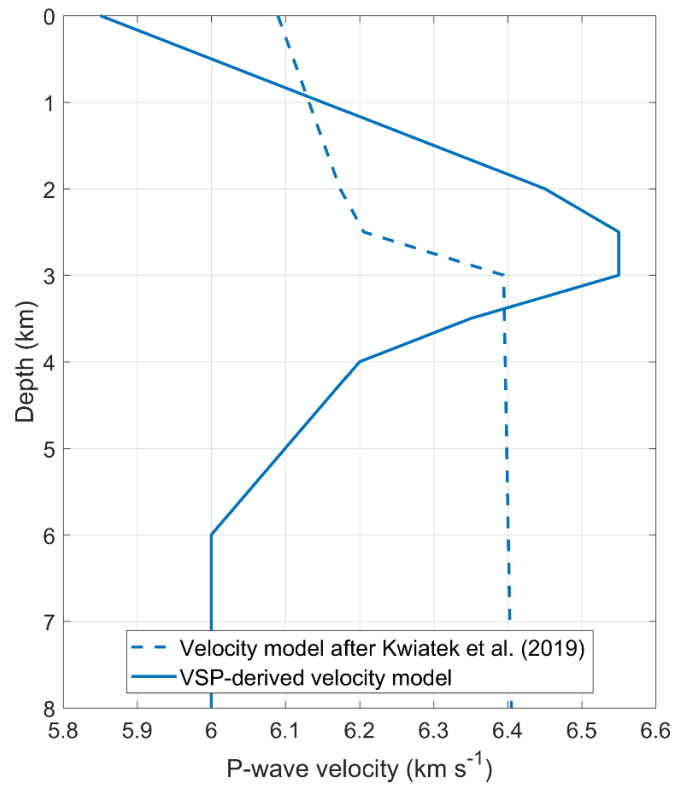
- Ader, T., Chendorain, M., Free, M., Saarno, T., Heikkinen, P., Malin, P., Leary, P., Kwiatek, G., Dresen, G., Bluemle, F., and Vuorinen, T.: Design and implementation of a traffic light system for deep geothermal well stimulation in Finland, *Journal of Seismology*, <https://doi.org/10.1007/s10950-019-09853-y>, 2019.
- 510 Bentz, S., Kwiatek, G., Martínez-Garzón, P., Bohnhoff, M., and Dresen, G.: Seismic mMoment eEvolution dDuring hHydraulic sStimulations, *Geophysical Research Letters*, 47, e2019GL086185, <https://doi.org/10.1029/2019GL086185>, 2019.
- Bohnhoff, M., Malin, P., ter Heege, J., Deflandre, J.-P., and Sicking, C.: Suggested best practice for seismic monitoring and characterization of non-conventional reservoirs, *First Break*, 36, 2, 59–64, 2018.
- 515 D’Auria, L. and Massa, B.: Stress iInversion of fFocal mMechanism dData uUsing a bBayesian aApproach: A nNovel fFormulation of the rRight tTrihedra mMethod, *Seismological Research Letters*, 86, 1–10, <https://doi.org/10.1785/0220140153>, 2015.
- Deichmann, N. and Giardini, D.: Earthquakes iInduced by the sStimulation of an eEnhanced gGeothermal sSystem below Basel (Switzerland), *Seismological Research Letters*, 80, 784–798, 520 <https://doi.org/10.1785/gssrl.80.5.784>, 2009.
- Diehl, T., Kraft, T., Kissling, E., and Wiemer, S.: The induced earthquake sequence related to the St. Gallen deep geothermal project (Switzerland): Fault reactivation and fluid interactions imaged by microseismicity, *Journal of Geophysical Research: Solid Earth*, 122, 7272–7290, <https://doi.org/10.1002/2017JB014473>, 2017.
- 525 Efron, B.: The jackknife, the bootstrap, and other resampling plans, Siam, 1982.
- Ellsworth, W.L.: Injection-iInduced eEarthquakes, *Science*, 341, 1225942, <https://doi.org/10.1126/science.1225942>, 2013.
- Ellsworth, W.L., Giardini, D., Townend, J., Ge, S., and Shimamoto, T.: Triggering of the Pohang, Korea, eEarthquake (Mw 5.5) by eEnhanced gGeothermal sSystem sStimulation, *Seismological Research* 530 *Letters*, 90, 1844–1858, <https://doi.org/10.1785/0220190102>, 2019.
- Font, Y., Kao, H., Lallemand, S., Liu, C.-S., and Chiao, L.-Y.: Hypocentre determination offshore of eastern Taiwan using the mMaximum iIntersection method, *Geophysical Journal International*, 158, 655–675, <https://doi.org/10.1111/j.1365-246X.2004.02317.x>, 2004.
- Galis, M., Pelties, C., Kristek, J., Moczo, P., Ampuero, J.-P., and Mai, P.M.: On the initiation of sustained slip- 535 weakening ruptures by localized stresses, *Geophysical Journal International*, 200, 890–909, <https://doi.org/10.1093/gji/ggu436>, 2015.

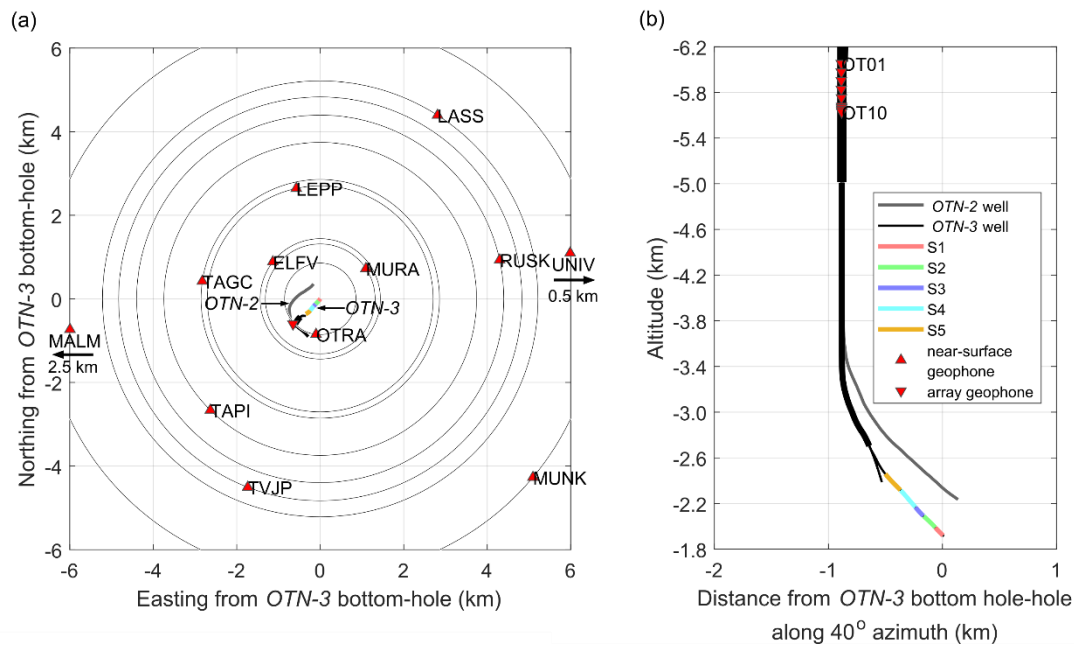
- Giardini, D.: Geothermal quake risks must be faced, *Nature*, 462, 848–849, <https://doi.org/10.1038/462848a>, 2009.
- Hanks, T.C. and Kanamori, H.: A moment magnitude scale, *Journal of Geophysical Research: Solid Earth*, 84, 2348–2350, <https://doi.org/10.1029/JB084iB05p02348>, 1979.
- ~~Hardebeck, J. and Shearer, P.: A New Method for Determining First Motion Focal Mechanisms, *Bulletin of the Seismological Society of America*, 92, 2264–2276, <https://doi.org/10.1785/0120010200>, 2002.~~
- Hardebeck, J.L. and Michael, A.J.: Damped regional-scale stress inversions: Methodology and examples for southern California and the Coalinga aftershock sequence, *Journal of Geophysical Research: Solid Earth*, 111, B11310, <https://doi.org/10.1029/2005JB004144>, 2006.
- ~~Hardebeck, J. and Shearer, P.: A nNew mMethod for dDetermining fFirst-mMotion fFocal mMechanisms, *Bulletin of the Seismological Society of America*, 92, 2264–2276, <https://doi.org/10.1785/0120010200>, 2002.~~
- Heidbach, O., Mojtaba, R., Reiter, K., Ziegler, M., and WSM Team: World sStress mMap dDatabase rRelease 2016 V.1.1, GFZ Data Services, <https://doi.org/10.5880/WSM.2016.001>, 2016.
- Hillers, G., Vuorinen, T., Uski, M., Kortström, J., Mäntyniemi, P., Tiira, T., Malin, P., and Saarno, T.: The 2018 gGeothermal rReservoir sStimulation in Espoo/Helsinki, sSouthern Finland: Seismic nNetwork aAnatomy and dData fFeatures, *Seismological Research Letters*, 91 (2A), 770–786, <https://doi.org/10.1785/0220190253>, 2020.
- Hofmann, H., Zimmermann, G., Farkas, M., Huenges, E., Zang, A., Leonhardt, M., Kwiatek, G., Martinez-Garzon, P., Bohnhoff, M., Min, K.-B., Fokker, P., Westaway, R., Bethmann, F., Meier, P., Yoon, K.S., Choi, J.W., Lee, T.J., and Kim, K.Y.: First field application of cyclic soft stimulation at the Pohang Enhanced Geothermal System site in Korea, *Geophysical Journal International*, 217, 926–949, <https://doi.org/10.1093/gji/ggz058>, 2019.
- Kagan, Y.Y.: 3-D rotation of double-couple earthquake sources, *Geophysical Journal International*, 106, 709–716, <https://doi.org/10.1111/j.1365-246X.1991.tb06343.x>, 1991.
- Kagan, Y.Y.: Simplified algorithms for calculating double-couple rotation, *Geophysical Journal International* 171, 411–418, <https://doi.org/10.1111/j.1365-246X.2007.03538.x>, 2007.
- Kakkuri, J. and Chen, R.: On horizontal crustal strain in Finland, *Bulletin Géodésique*, 66, 12–20, <https://doi.org/10.1007/BF00806806>, 1992.

- Kwiatek, G., Bohnhoff, M., Martínez-Garzón, P., Bulut, F., and Dresen, G.: High-resolution reservoir characterization using induced seismicity and state of the art waveform processing techniques, *First Break*, 31, 81-88, <https://doi.org/0.3997/1365-2397.31.7.70359>, 2013.
- 570 Kwiatek, G., Martínez-Garzón, P., Dresen, G., Bohnhoff, M., Sone, H., and Hartline, C.: Effects of long-term fluid injection on induced seismicity parameters and maximum magnitude in northwestern part of The Geysers geothermal field, *Journal of Geophysical Research: Solid Earth*, 120, 7085–7101, <https://doi.org/10.1002/2015JB012362>, 2015.
- 575 Kwiatek, G., Saarno, T., Ader, T., Bluemle, F., Bohnhoff, M., Chendorain, M., Dresen, G., Heikkinen, P., Kukkonen, I., Leary, P., Leonhardt, M., Malin, P., Martínez-Garzón, P., Passmore, K., Passmore, P., Valenzuela, S., and Wollin, C.: Controlling fluid-induced seismicity during a 6.1-km-deep geothermal stimulation in Finland, *Science Advances*, 5, eaav7224, <https://doi.org/10.1126/sciadv.aav7224>, 2019.
- Lagarias, J.C., Reeds, J.A., Wright, M.H., and Wright, P.E.: Convergence **p**Properties of the Nelder--Mead **s**Simplex **m**Method in **l**ow **d**Dimensions, *SIAM J. Optim.*, 9, 112–147, <https://doi.org/10.1137/S1052623496303470>, 1998.
- 580 <https://doi.org/10.1137/S1052623496303470>, 1998.
- Lomax, A.: A **r**eanalysis of the **h**ypocentral **l**ocation and **r**elated **o**bservations for the **g**reat 1906 California **e**arthquake, *Bulletin of the Seismological Society of America*, 95, 861–877, <https://doi.org/10.1785/0120040141>, 2005.
- Lund, B. and Townend, J.: Calculating horizontal stress orientations with full or partial knowledge of the tectonic stress tensor, *Geophysical Journal International*, 170, 1328–1335, <https://doi.org/10.1111/j.1365-246X.2007.03468.x>, 2007.
- 585 <https://doi.org/10.1111/j.1365-246X.2007.03468.x>, 2007.
- [Majer, E., Nelson, J., Robertson-Tait, A., Savy, J., and Wong, I.: Protocol for addressing induced seismicity associated with enhanced geothermal systems, US Department of Energy, DOE EE-0662, 2012.](#)
- Martínez-Garzón, P., Bohnhoff, M., Kwiatek, G., and Dresen, G.: Stress tensor changes related to fluid injection at The Geysers geothermal field, California, *Geophysical Research Letters*, 40, 2596–2601, <https://doi.org/10.1002/grl.50438>, 2013.
- 590 <https://doi.org/10.1002/grl.50438>, 2013.
- Martínez-Garzón, P., Kwiatek, G., Bohnhoff, M., and Ickrath, M.: MSATSI: A MATLAB **p**ackage for **s**tress **i**nversion **c**ombining **s**olid **c**lassic **m**ethodology, a **n**ew **s**implified **u**ser-**h**andling, and a **v**isualization **f**ool, *Seismological Research Letters*, 85, 896–904, <https://doi.org/10.1785/0220130189>, 2014.
- 595 2014.
- Martínez-Garzón, P., Vavryčuk, V., Kwiatek, G., and Bohnhoff, M.: Sensitivity of stress inversion of focal mechanisms to pore pressure changes, *Geophysical Research Letters*, 43, 8441–8450, <https://doi.org/10.1002/2016GL070145>, 2016.

- Maxwell, S. C., Shemeta, J., Campbell, E., and Quirk, D.: Microseismic deformation rate monitoring, in: SPE  
600 Annual Technical Conference and Exhibition, edited, pp. 4185–4193, Denver, Colorado:  
Society of Petroleum Engineers, 2008.
- Nelder, J.A. and Mead, R.: A **s**implex **m**ethod for **f**unction **m**inimization, The Computer Journal, 7, 308–  
313, <https://doi.org/10.1093/comjnl/7.4.308>, 1965.
- Rubinstein, J.L. and Ellsworth, W.L.: Precise estimation of repeating earthquake moment: Example from  
605 **P**arkfield, California, Bulletin of the Seismological Society of America, 100, 1952–1961,  
<https://doi.org/10.1785/0120100007>, 2010.
- Shelly, D.R., Hardebeck, J.L., Ellsworth, W.L., and Hill, D.P.: A new strategy for earthquake focal mechanisms  
using waveform-correlation-derived relative polarities and cluster analysis: Application to the 2014  
Long Valley Caldera earthquake swarm, Journal of Geophysical Research: Solid Earth, 121, 8622–  
610 8641, <https://doi.org/10.1002/2016JB013437>, 2016.
- Tape, W. and Tape, C.: Angle between principal axis triples, Geophysical Journal International, 191, 813–831,  
<https://doi.org/10.1111/j.1365-246X.2012.05658.x>, 2012.
- Vavryčuk, V.: Principal earthquakes: Theory and observations from the 2008 West Bohemia swarm, Earth and  
Planetary Science Letters, 305, 290–296, <https://doi.org/10.1016/j.epsl.2011.03.002>, 2011.
- 615 Vavryčuk, V.: Iterative joint inversion for stress and fault orientations from focal mechanisms, Geophysical  
Journal International, 199, 69–77, <https://doi.org/10.1093/gji/ggu224>, 2014.
- Waldhauser, F. and Ellsworth, W.L.: A **d**ouble-**d**ifference **e**arthquake **l**ocation **a**lgorithm: Method and  
**a**pplication to the Northern Hayward Fault, California, Bulletin of the Seismological Society of  
America, 90, 1353–1368, <https://doi.org/10.1785/0120000006>, 2000.
- 620 Zhou, H.: Rapid three-dimensional hypocentral determination using a master station method, Journal of  
Geophysical Research: Solid Earth, 99, 15439–15455, <https://doi.org/10.1029/94JB00934>, 1994.

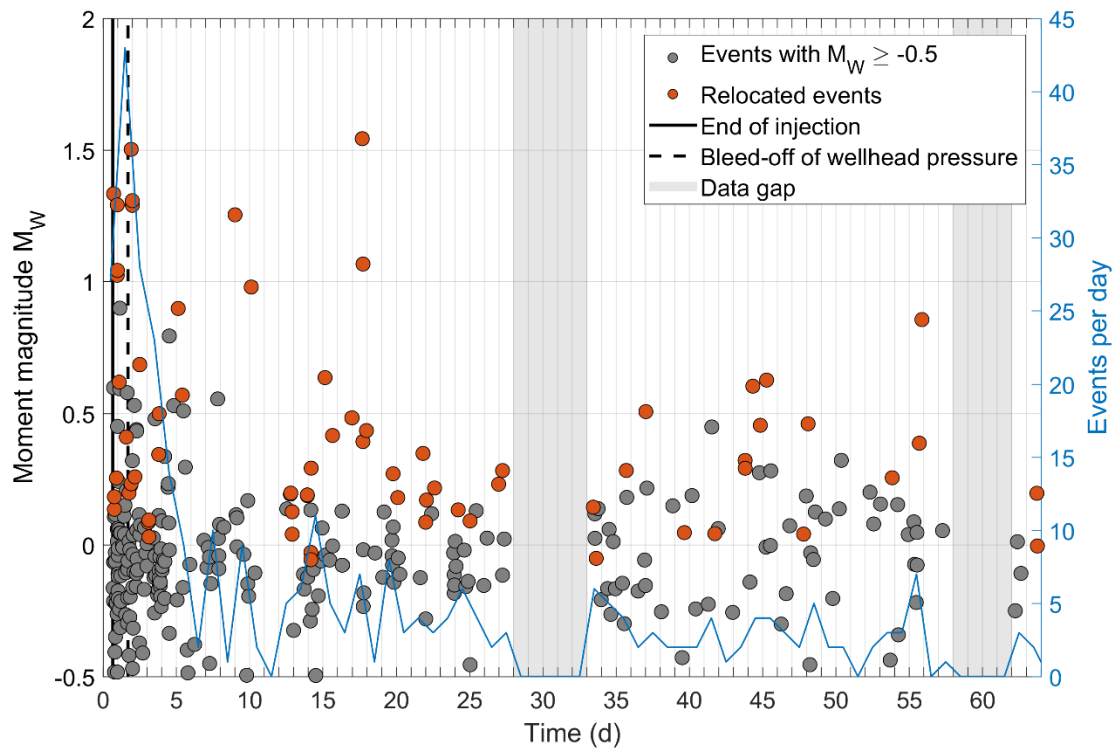
## Figures

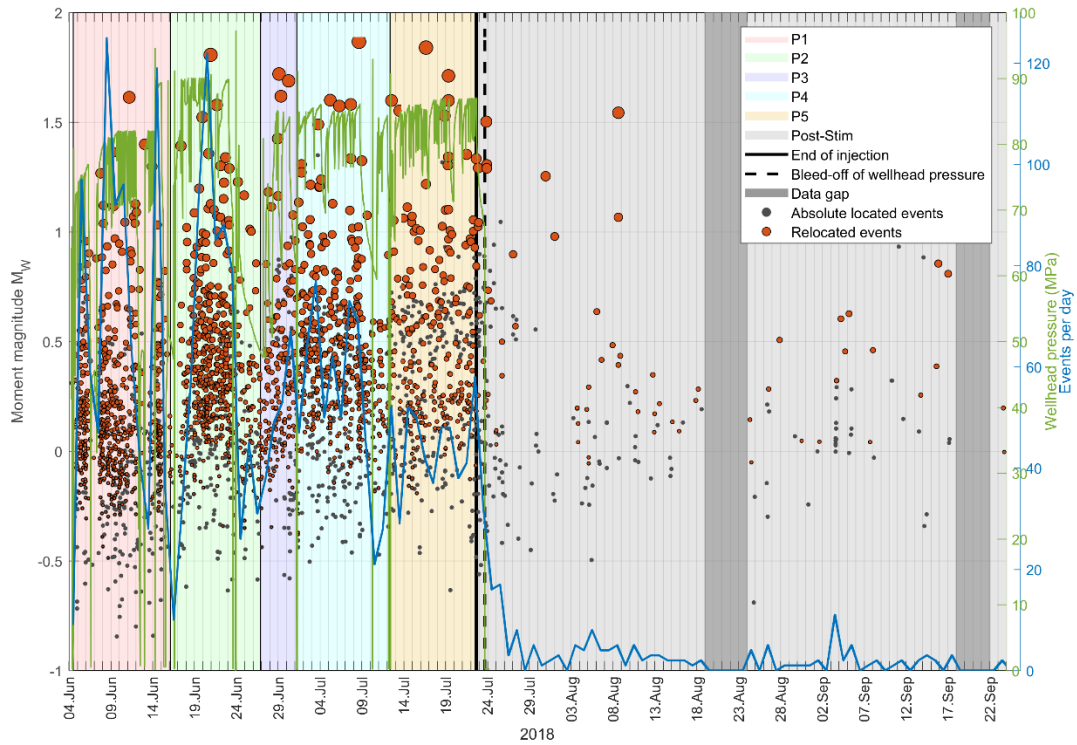




625 **Figure 1. Comparison of the updated 1D-layered velocity model derived from calibration shots of VSP campaign (solid line) with the 1D-layered velocity model used in Kwiatek et al. (2019) (dashed line). Seismic network used for monitoring the stimulation in 2018. (a) Map view showing the near-surface geophones framing the EGS site with the injection borehole OTN-3 and the OTN-2 well drilled in 2019 and 2020. Radius of concentric circles presents distance between the end of the OTN-3 borehole and each station. (b) Side view of the boreholes with the geophone-array placed at the already existing part of the OTN-2 well. The injection intervals S1-S5 of the stimulation in 2018 are color-coded at the end of the injection borehole. For further details about location of the EGS site at the suburban area of Helsinki in Finland see Kwiatek et al. (2019).**

630

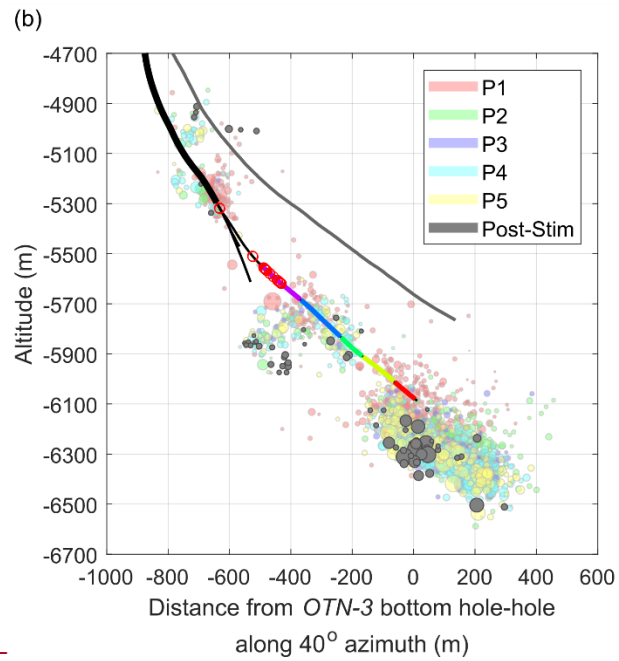
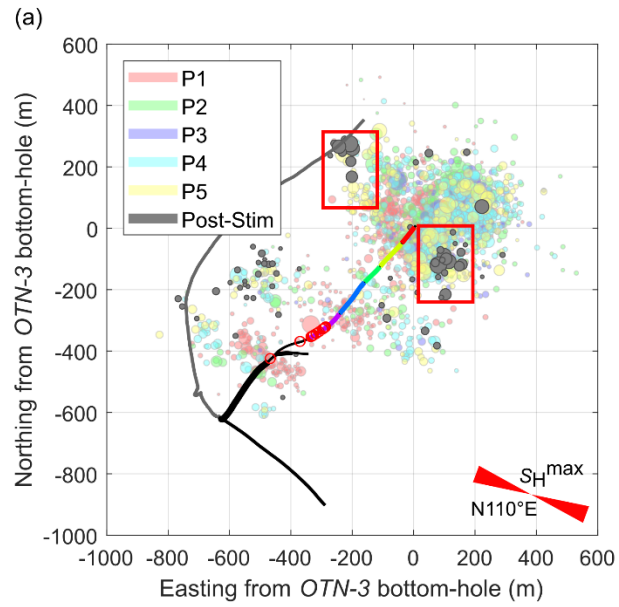


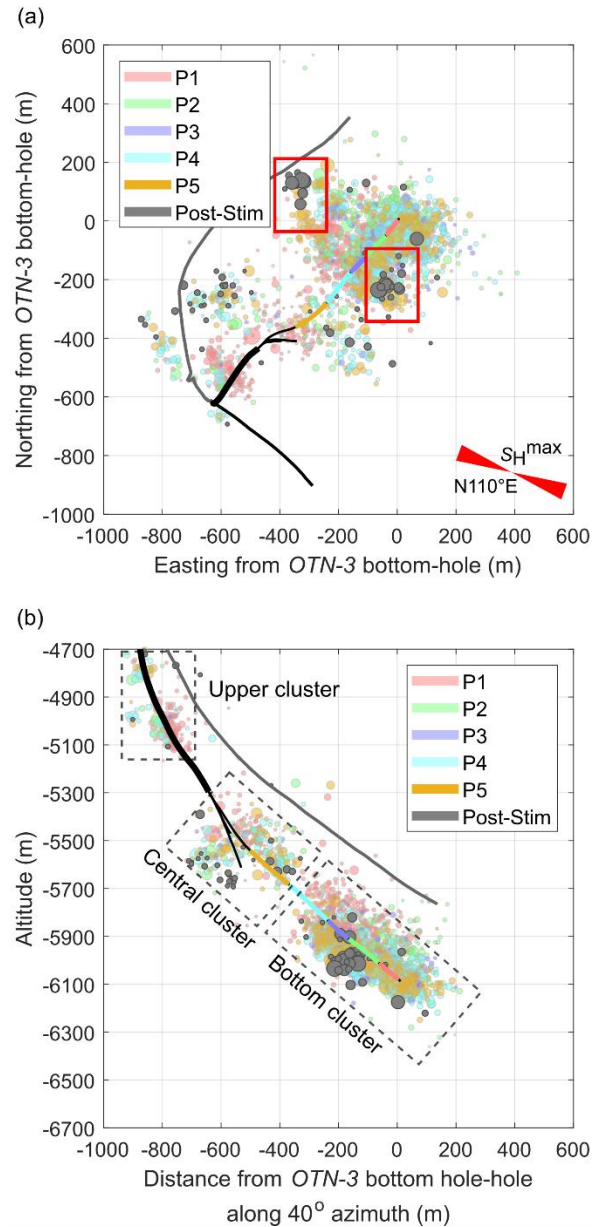


635

**Figure 2. Stimulation protocol with moment magnitudes of induced seismicity during stimulation phases P1-P5 and post-stimulation time period. The magnitudes of absolute located and relocated events are shown as grey and orange dots, respectively. The green solid line presents the wellhead pressure during the stimulation. The seismic event rate per day is shown by the solid blue line. Post-stimulation seismicity plotted with time. Events with  $M_w \geq -0.5$  and relocated events are plotted as grey and orange dots, respectively.**

640

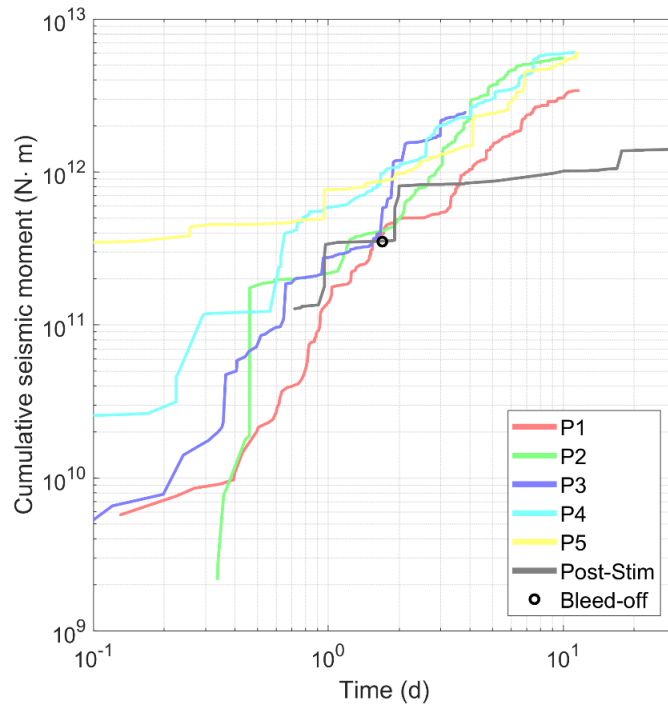




645

Figure 3. Hypocenters of relocated events. (a) Map view and (b) SW-NE depth section. The hypocenters are color-coded with the stimulation phases (cf. Kwiatek et al., 2019) and size corresponds to moment magnitude. Relocated seismicity that occurred after the stimulation is represented as grey dots. Areas with large events occurring during stimulation phase P5 and post-stimulation time are highlighted by red rectangles (see main text for details). The five injection stages are marked as color bands along the borehole trace from the bottom of the open-hole toward the casing shoe of the injection well OTN-3 (black). The new OTN-2 well (grey) was drilled in 2019 to 2020 after the stimulation.





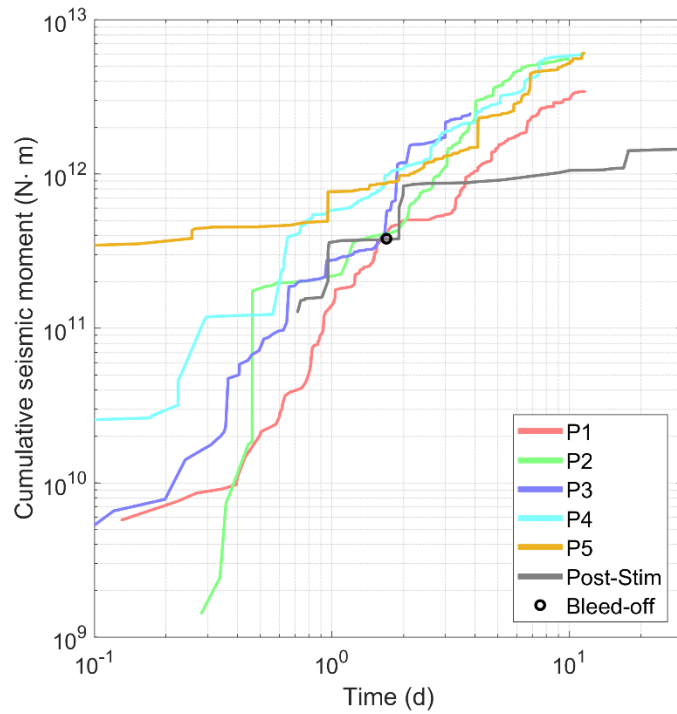
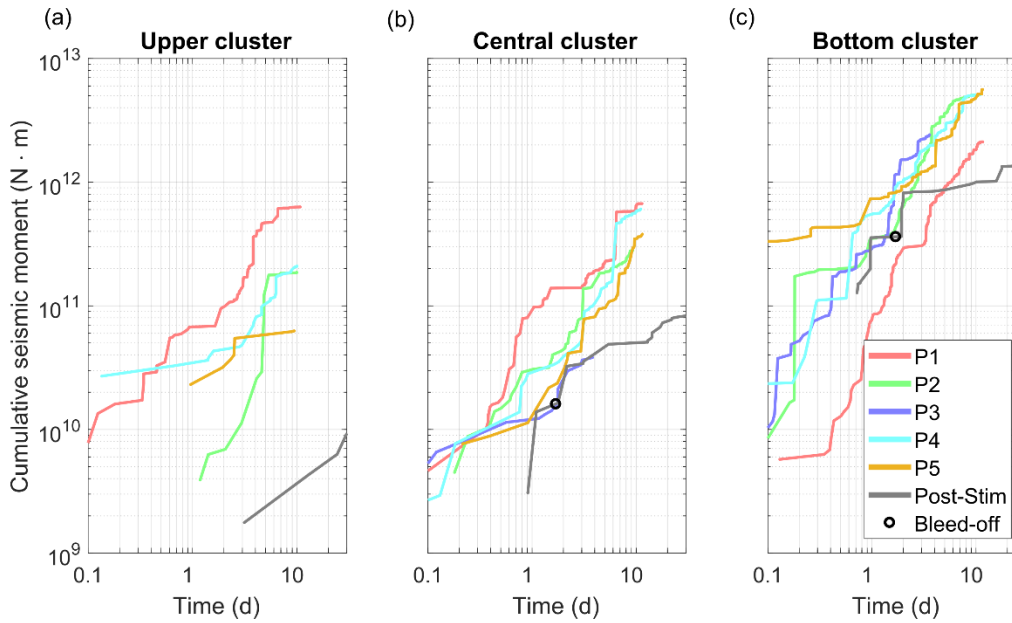
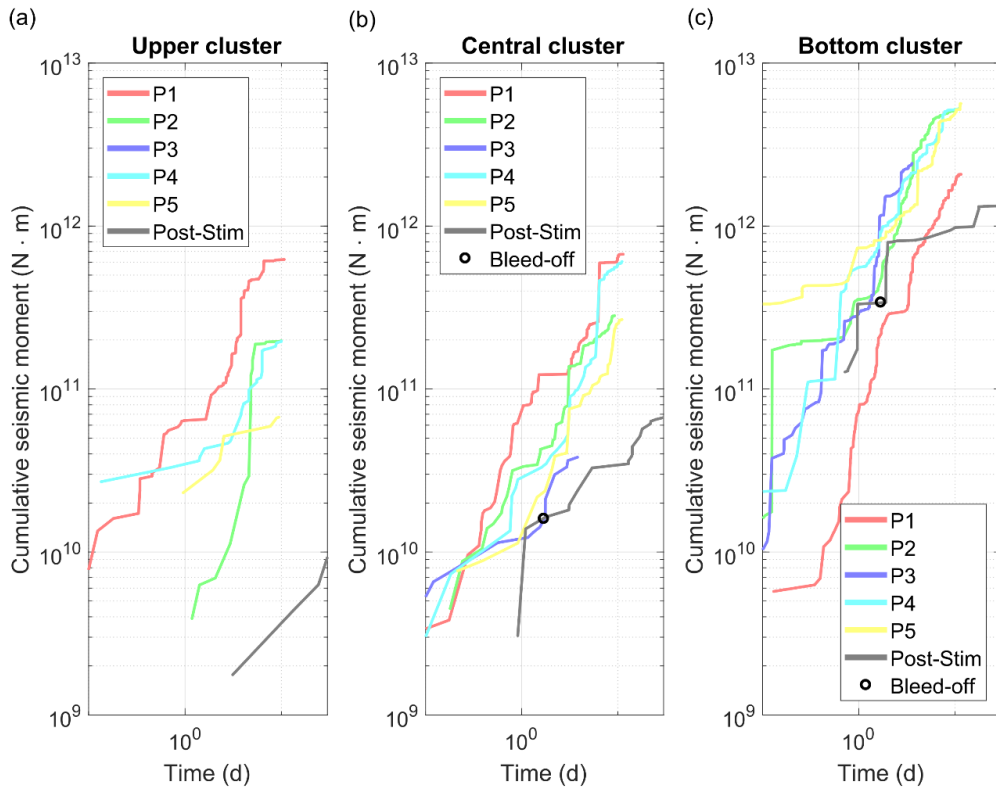
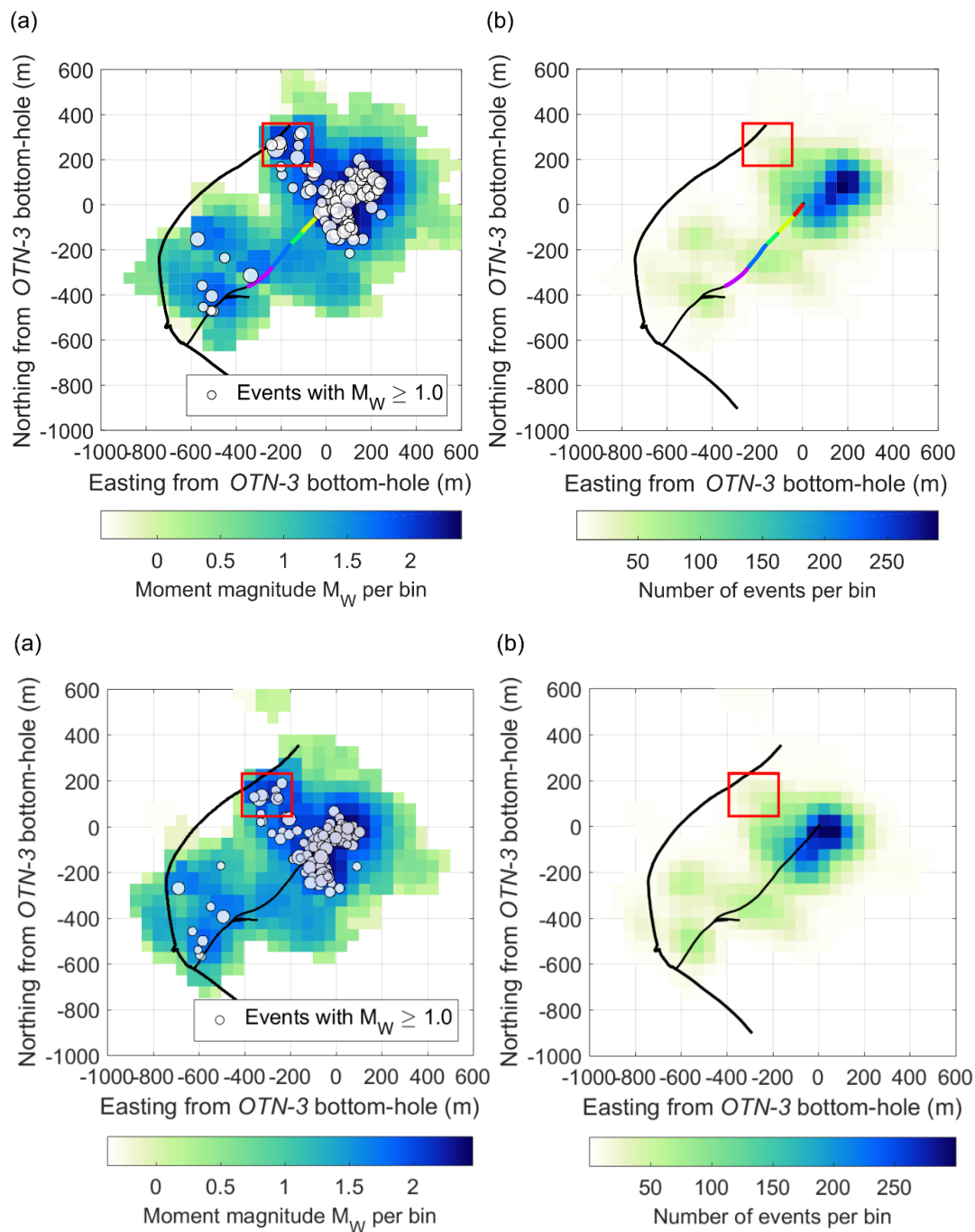


Figure 4. For a time period of 30 days, the tTemporal evolution of cumulative seismic moment release for the relocated seismicity is shown since the beginning for each injection phase as well as for the post-stimulation phase.



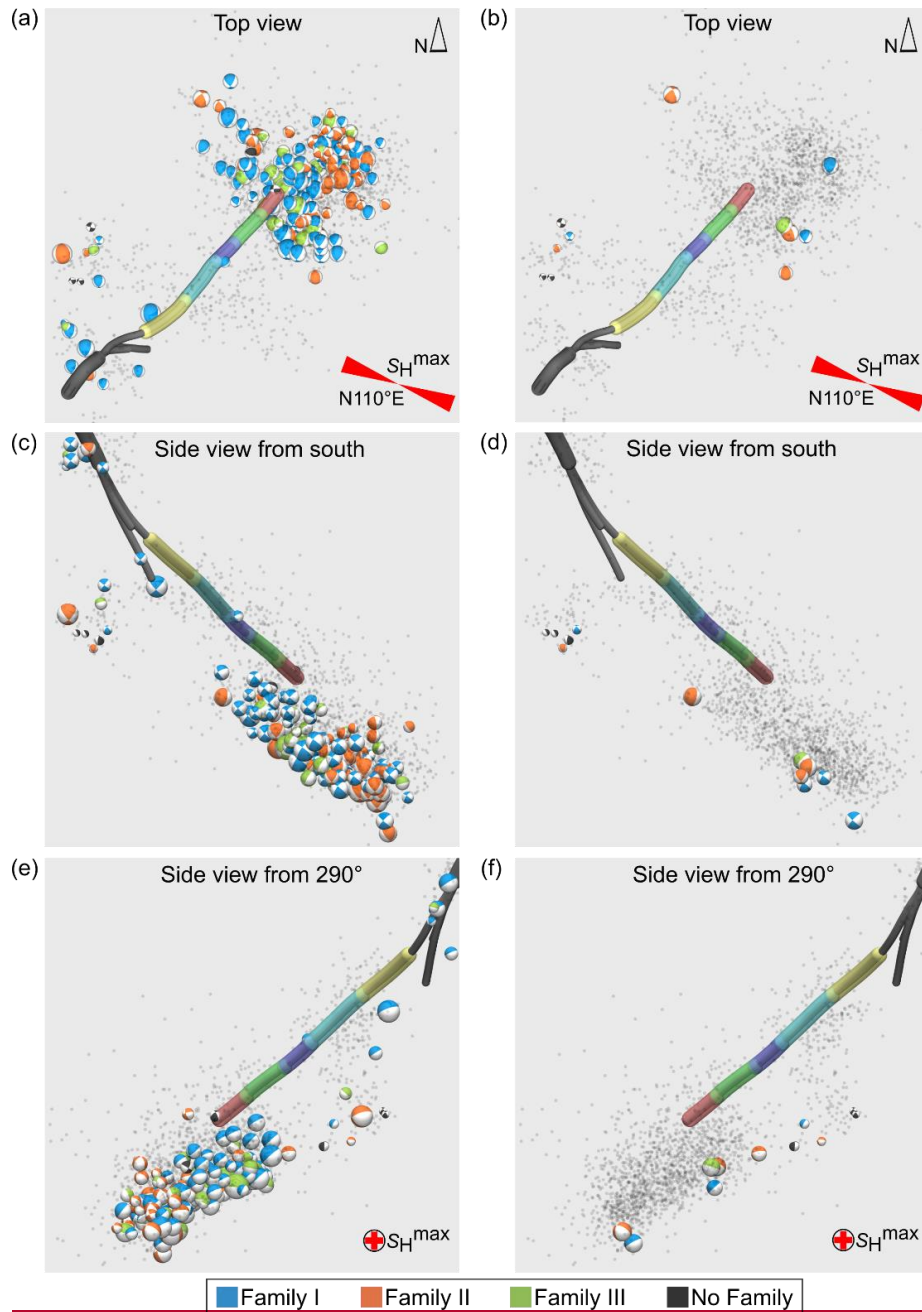
660 **Figure 5. Temporal evolution of the cumulative seismic moment release with time for each of the three hypocenter clusters separately: (a) The uppermost hypocenter cluster, (b) the central hypocenter cluster and (c) the deepest and main hypocenter cluster.**

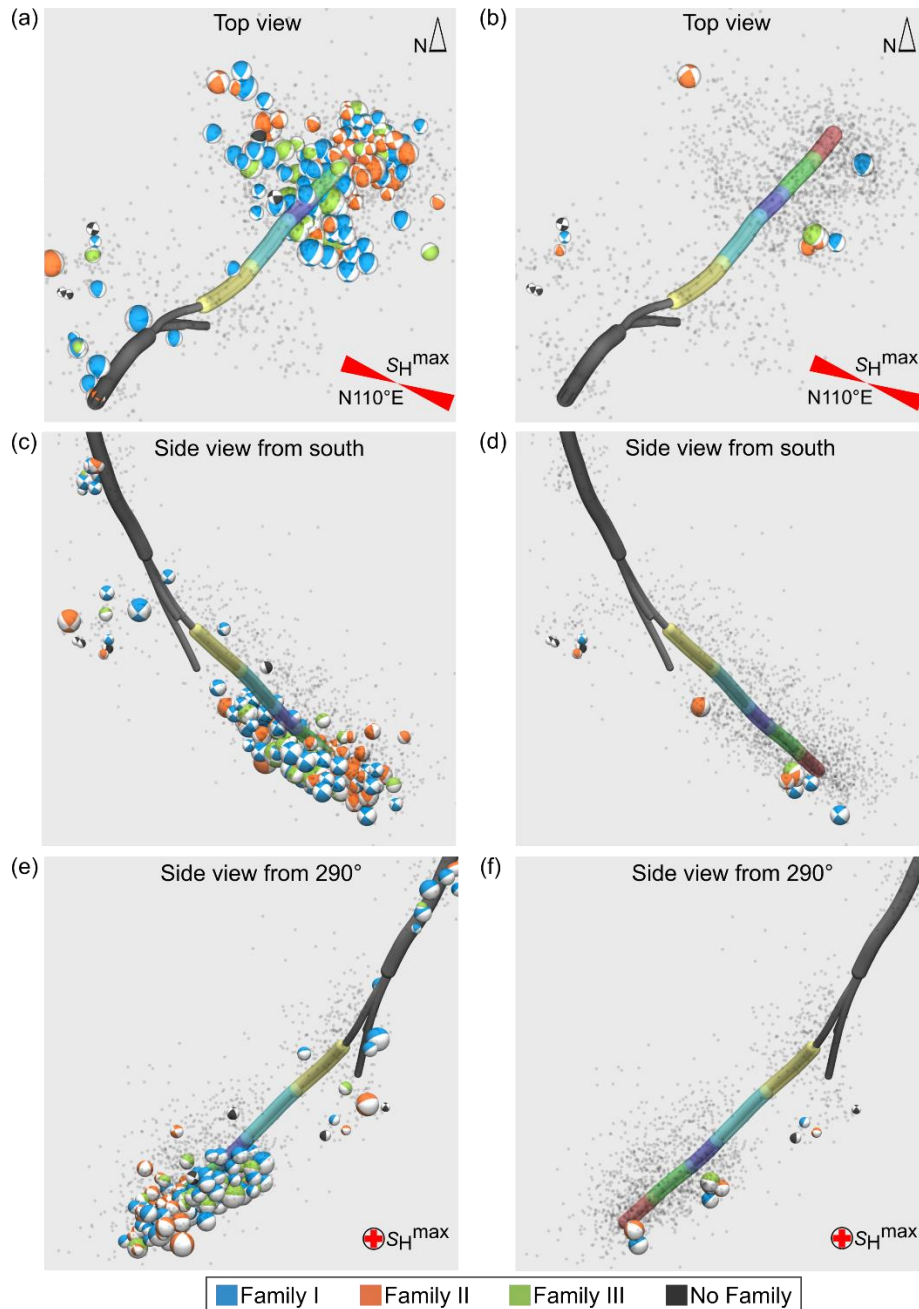


665 **Figure 6. Spatial evolution of the cumulative seismic moment release of the relocated seismicity per bins of 50-by-50 m.**  
 (a) **The cumulative seismic moment release converted to seismic moment magnitude per bin overlaid by seismicity with**

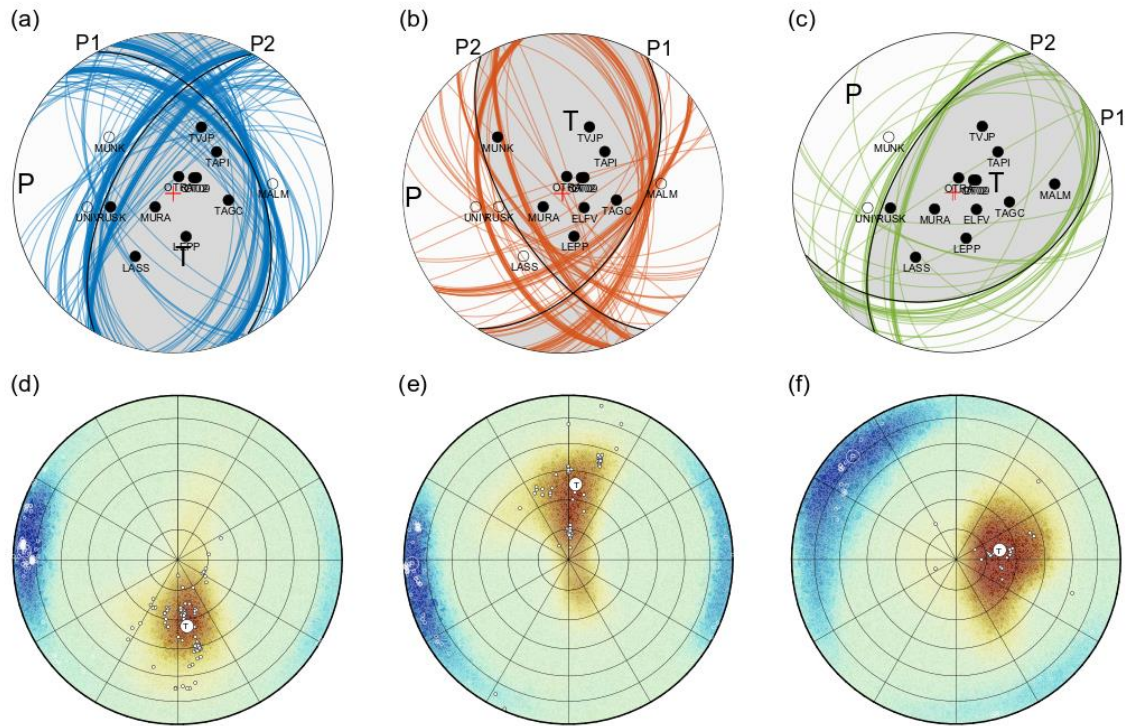
$M_w \geq 1$ . (b) The number of events that occurred per bin. A smaller area of anomalously high  $CM_0$  release caused by a few large events is highlighted by red rectangle.

670

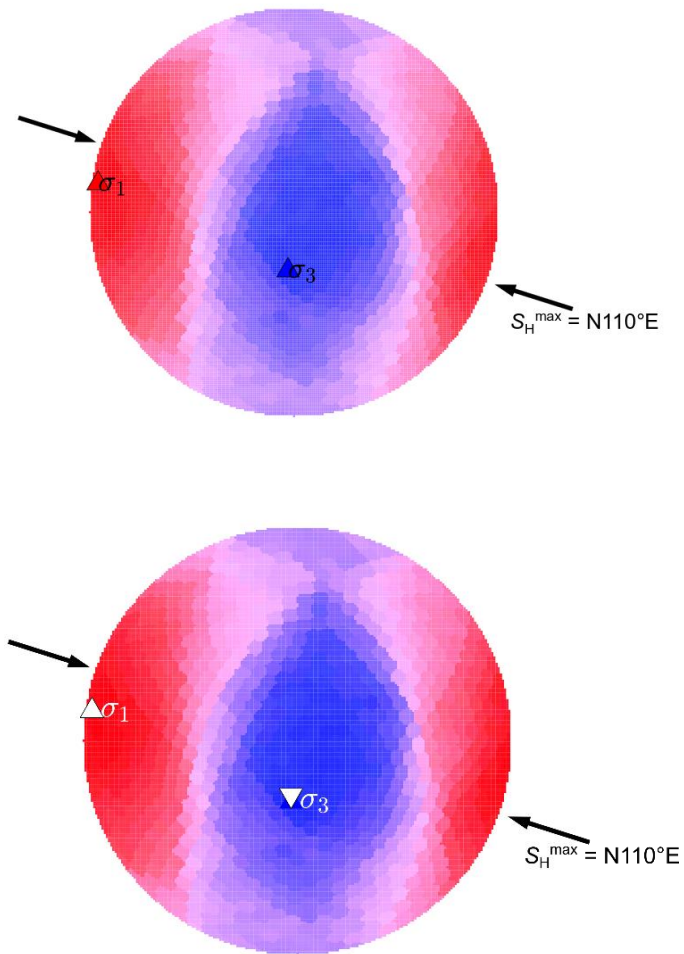




675 **Figure 7. Orthogonal views of estimated focal mechanisms in three different projections: (a, b) map view, (c, d) side view from south (180°) as well as (e, f) side view from NW (290°), along the direction of the maximum horizontal stress  $S_H^{\max} = 110^\circ$ . (a, c, e): All 191 estimated focal mechanisms. (b, d, f): Focal mechanisms of post-stimulation events. Color-code indicating family obtained. Relocated seismicity without estimated focal mechanisms are plotted with grey small dots.**

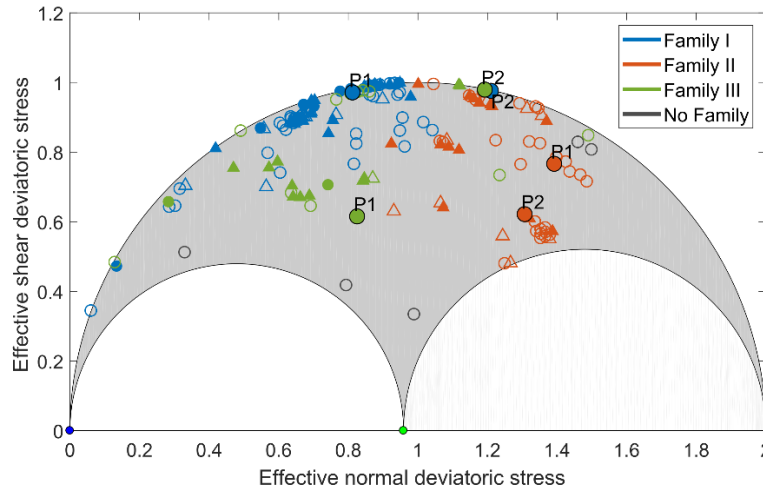
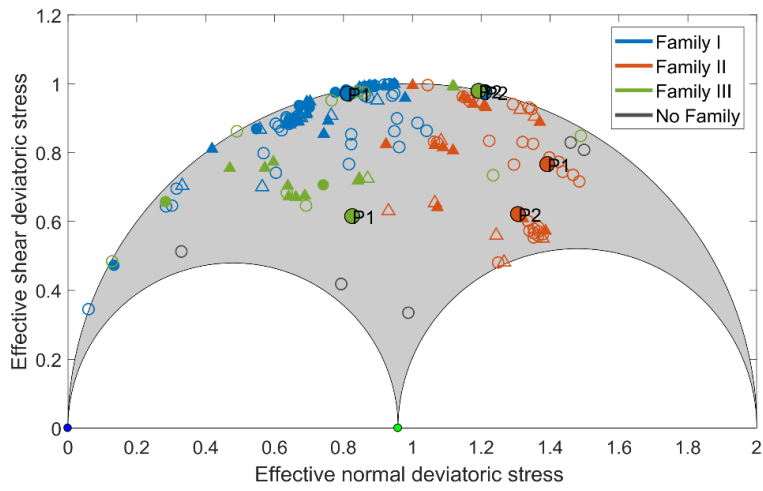


680 Figure 8. (a-c): Mean fault plane solutions (black lines) calculated from best FPSs of events forming family I  
 (a), family II (b) and family III (c). Contributing FPSs from which mean is calculated are shown with blue, orange and  
 685 green color, respectively. The most repetitive polarity pattern observed at each station is presented as black or white  
 dot for positive or negative onsets, respectively. P1 and P2 symbols correspond to the projections of main and auxiliary  
 fault planes according to which one is better oriented for failure on the Mohr circle represented in Fig. 10. (d-f):  
 For each of the families, the mean P- and T-axes as well as axes of contributing FPSs are plotted with big and small white  
 dots, respectively. The *HASH*-derived uncertainties (95 % confidence interval) of the P- and T-axis of all events within  
 each family are shown using blue and brown coloring scale, respectively.



690

Figure 9. Stereonet of the estimated local stress field using *BRTM* method. WhiteRed and blue upward and downward pointing triangles represent maximum and minimum principal stress axes  $\sigma_1$  and  $\sigma_3$ , respectively. Black arrows represent maximum horizontal stress  $S_H^{\max}$  in the reservoir.



695

700

Figure 10. Deviatoric Mohr circle representing the local stress field with the fault plane solutions having the highest fault instability coefficient of the estimated focal mechanisms. A stress ratio of  $R = 0.53$  was used for stress inversion. Events with  $M_w \geq 1$  and  $M_w < 1$  are plotted as triangles and circles, respectively. Filled and unfilled markers represent events with manually picked and estimated polarities, respectively. The mean and its auxiliary fault plane solution of each family are plotted as filled large dots labelled with P1 and P2, respectively. Most family I events (blue symbols) occurred on critically stressed faults.

## Data publication related to

# “Seismicity during and after stimulation of a 6.1 km deep Enhanced Geothermal System in Helsinki, Finland”

Maria Leonhardt, Grzegorz Kwiatek, Patricia Martínez-Garzón, Pekka Heikkinen

### 1. Structure of seismic catalog file

Column 1:

ID number of event

If events were detected but not located, the ID is 0.

Column 2:

Datenummer (integer part = day since year 0)

Column 3-8:

Year, month, day, hour, minute, second

Column 9:

Local “Helsinki” magnitude  $M_{LHEL}$

Column 10:

Moment magnitude  $M_W$

Column 11-13:

Easting (m), northing (m), altitude (m) of absolute location

Column 14-16:

Easting (m), northing (m), altitude (m) of relocation

Column 17-19:

Strike, dip, rake of preferred nodal plane from estimated focal mechanisms

Column 20:

Root mean square fault plane uncertainties of estimated focal mechanisms

For further details about the reprocessing of the catalog and its properties, please see section 2 and 3 below.

## 2. Seismic catalog development

The original seismic catalog created during stimulation campaign has been reprocessed by Kwiatek et al. (2019), and included 6,150 located and ~54,000 detected earthquakes.

In first step, this catalog was extended in time to cover the post-stimulation period of 63 days. In the following, we selected best quality 5,456 events that were located during and after the stimulation, and reprocessed them in our study, as discussed in details below. The original catalog of detections was reviewed as well, resulting in 55,707 smaller events detected during and after the stimulation. Thus the total seismic catalog presented in this data publication contains 61,163 earthquakes in the period of 112 days that occurred in the vicinity of the *OTN-3* well. In the following sections we present the development of seismic catalog.

### 2.1 Seismic network

Following Kwiatek et al., (2019), the real-time telemetered network monitoring the stimulation campaign was composed of 24 borehole seismographs, fabricated, installed, and operated by Advanced Seismic Instrumentation and Research ([www.asirseismic.com](http://www.asirseismic.com)). The 12-level borehole array of three-component 15-Hz natural frequency Geospace OMNI-2400 geophones was sampled at 2 kHz and placed at depths of 1.95 to 2.37 km in the *OTN-2* well. Additional 12-station three-component  $f_N = 4.5$  Hz Sunfull PSH geophones sampled at 500 Hz were installed in 0.30- to 1.15-km-deep wells. These surrounded the project site at 0.6- to 8.2-km epicentral distances. These two networks were operating months before the start of stimulation with no event detected in the vicinity of *OTN-3* injection well. Data from these 24 sensors were used in processing of seismic data forming the data publication.

### 2.2 Detection catalog

We followed the same approach as presented in Kwiatek et al. (2019). P-wave arrivals unused in locations, but detected using the array located in *OTN-2* well, were further analyzed. Assuming that a small event that is detected solely at the *OTN-2* array must occur in its immediate vicinity, we placed a hypothetical seismic source at the bottom of *OTN-3* where the injection took place. We then calculated travel times of P-waves to the sensors forming the *OTN-2* array, obtaining a particular pattern (offset) of expected P-wave arrivals at these stations. We then scanned the catalog of unused *OTN-2* P-wave arrivals for this particular pattern, and each matching set of detections was attributed to an event occurring in the vicinity of the *OTN-3* well. The magnitude (see section 2.5) was calculated assuming that the event occurred at the bottom of the *OTN-3* injection well. This procedure allowed us to enhance the catalog by 55,707 earthquakes.

### 2.3 VSP-based velocity model

In original study of Kwiatek et al. (2019), the 1D velocity model based on velocity logs was used. In the study of Leonhardt et al. (2020), the new velocity model was developed from P-wave onset times of calibration shots obtained during a post-injection Vertical Seismic Profiling (VSP) campaign.

The VSP campaign was performed in October 2018 after the end of the stimulation. Overall, 47 calibration shots were performed at 7 shot points located around the injection well *OTN-3* with a maximum distance of less than 8 km. Shot points were prepared with explosives in holes up to 40 m depth. The VSP campaign was monitored by a

17-level vertical chain with 3-components geophones located in the injection well *OTN-3* in a depth between 2.5 km and 4.5 km. In addition, the 12-level vertical geophone chain, used for the stimulation, was also monitoring the VSP shots to cover the depth above 2.5 km.

The 1D velocity model used in Leonhardt et al. (2020) was developed from the data of VSP shot performed close to the OTRA station. This secured that wave propagation ray was nearly vertical between the shot location and seismic arrays. This allowed us to convert travel-path velocities calculated at different sensors forming the array along the *OTN-3* well to interval velocities of the 1D velocity model. For the depths below 4.5 km which was not covered by seismic rays of VSP shots we used information from sonic logs, available depth between 5.1 km and 6.4 km. The velocity model is presented in Fig. 1. Due to a low Signal-to-Noise (S/N) ratio of the VSP data, the S-wave arrival times could not be determined.

The 1D VSP-derived velocity model shows a velocity inversion between 3 and 6 km depth (Fig. 1). The maximum P-wave velocity is  $0.15 \text{ km s}^{-1}$  larger than the maximum velocity modelled by Kwiatek et al. (2019) where a constant velocity of  $6.4 \text{ km s}^{-1}$  starting at 3 km depth was assumed. Below the velocity inversion, approximately constant velocity of  $6 \text{ km s}^{-1}$  is suggested from sonic logs for the updated 1D velocity model (Fig. 1).

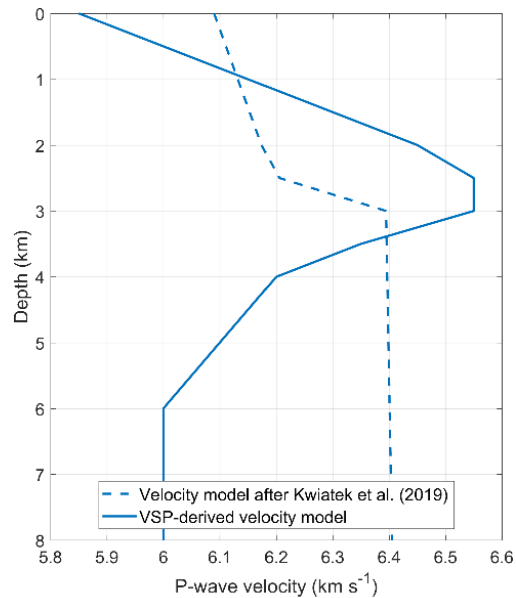


**Figure 1.** Comparison of 1D velocity model developed from VSP profiling (solid line) and the one used in Kwiatek et al. (2019).

## 2.4 Earthquake location and relocation

The sub-catalog of 5,456 events was reprocessed applying the new 1D layered velocity model. Thus, the  $V_P/V_S$  ratio had to be optimized by a trial-and-error procedure, as discussed in Leonhardt (2020). We found the optimum  $V_P/V_S$  by minimizing the cumulative residual errors of all located events while keeping first induced seismic events close to the

injection well *OTN-3*. The optimized  $V_p/V_s$  ratio of 1.71 was therefore selected which is similar to that used in Hillers et al. (2020).

The hypocenter locations were estimated using the Equal Differential Time (EDT) method (Zhou, 1994; Font et al., 2004; Lomax, 2005) and the new VSP-derived velocity model. In addition, station corrections were applied. The minimization of travel time residuals:

$$\left| (T_j^{th} - T_i^{th}) - (T_j^{obs} - T_i^{obs}) \right|_{L_2} = \min, \quad (1)$$

where  $T^{th}$  and  $T^{obs}$  are all unique pairs (i,j) of theoretical and observed travel times of P- and S-phases, were resolved using the Simplex algorithm (Nelder and Mead, 1965; Lagarias et al., 1998). A total of 2,958 reprocessed events were absolute located around the injection well *OTN-3* at an epicentral distance of less than 5 km and at depth of 4.5 to 7 km. The hypocenters of these events were included to the reprocessed and published catalog.

To further refine the quality of hypocenter locations, 2,178 from the 2,958 absolute located events with at least 10 P-wave and 4 S-wave picks were selected and the double-difference relocation technique (hypoDD) was applied using the new VSP-derived velocity model (Waldhauser and Ellsworth, 2000). An iterative least-square inversion was used to minimize residuals of observed and predicted travel time differences for event pairs calculated from the existing P- and S-wave picks of the selected catalog data. The residuals were minimized in ten iterations steps. For the last iteration, the maximum threshold for travel time residuals were set to 0.08 s and the maximum distance between the catalog linked event pairs was defined as 170 m. With the hypoDD method 1,986 events were relocated and thus 91 % of the selected 2,178 events. The residuals of the relocations have a root mean square error of 9 ms. The relocation uncertainties were then assessed using a bootstrap technique (Waldhauser and Ellsworth, 2000; Efron, 1982) leading to relative location precision not exceeding  $\pm 52$  m for 95 % of the catalog.

## 2.5 Basic source characteristics and statistical properties

Local ‘‘Helsinki’’ magnitude  $M_{LHEL}$  has been calculated from ground displacement seismograms integrated from ground velocity records (Uski and Tuppurainen, 1996; further updated by Uski et al. (2015) to smaller events). The magnitude was calculated separately on each station (24 sensors) using vertical component seismograms, and then averaged. The moment magnitudes of all events were estimated from local magnitudes  $M_{LHEL}$  using formula from Uski et al. (2015). The seismic moment was recalculated from  $M_W$  using formula of Hanks and Kanamori (1979).

The magnitude of completeness  $M_C$  as well as the  $b$ -value were calculated assuming a Gutenberg-Richter (GR) power law:  $\log_{10} N = a - bM_C$ , where  $N$  is the cumulative number of earthquakes with magnitudes larger than  $M_C$ . Following the Goodness-of-fit method (Wiemer and Wyss, 2000), the magnitude of completeness and the  $b$ -value were estimated assuming that the GR power law can fit 98 % of the seismic data.

## 3. Seismic catalog properties

The reprocessed seismic catalog covers the time period between 4<sup>th</sup> of June and 24<sup>th</sup> of September 2018. The stimulation was performed during the first 49 days. After shut-in of injection, i.e. after 22<sup>nd</sup> of July 2018 at 15:52 UTC, further 63 days of the post-stimulation time period were monitored.

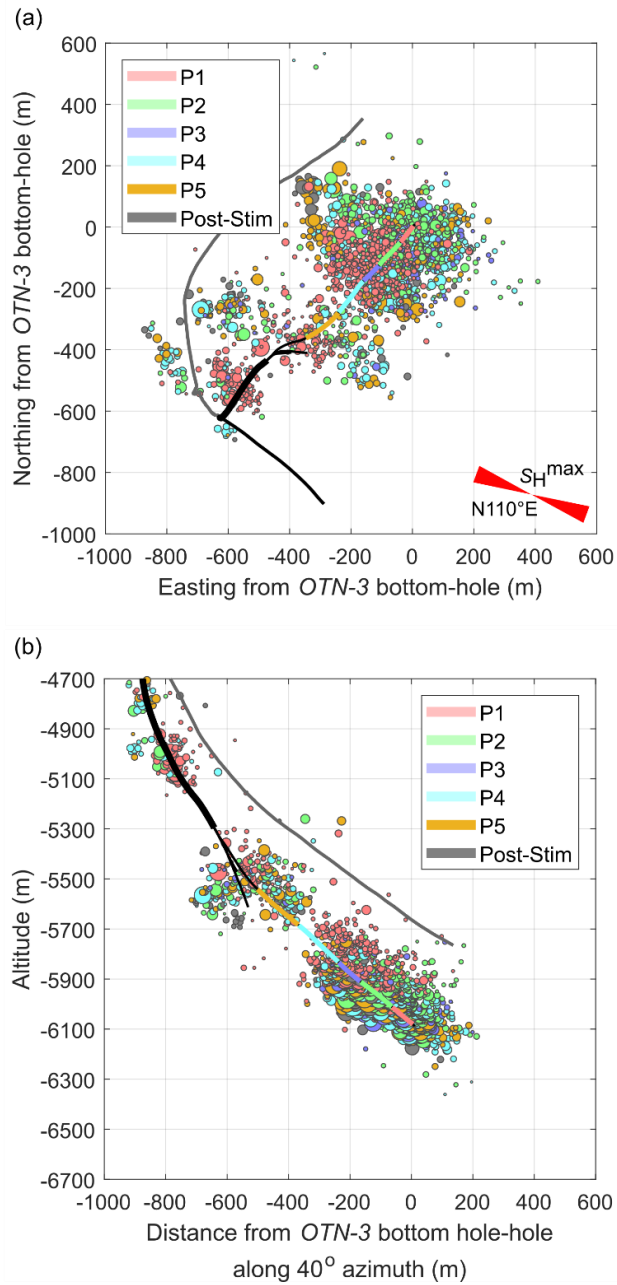
Overall, 61,163 earthquakes were detected during and after the stimulation. From the 55,707 events that were detected but not further processed, 52,107 detections occurred during the stimulation whereas another 3,600 detections were monitored after the stimulation. From the 5,456 events that were further processed, 4,510 events were monitored during and 946 events were monitored after the end of stimulation.

### **3.1 Moment magnitudes**

The 55,707 event detections, that were not further located or processed, had moment magnitudes between  $M_W = -0.95$  and  $M_W = 1.53$ . The subset of 2,958 events that were absolute located within the target volume around the injection well *OTN-3* with an epicentral distance of less than 5 km and a depth between 4.5 km and 7 km had moment magnitudes between  $M_W = -0.84$  and  $M_W = 1.87$ . The 213 post-injection events that were absolute located within the target volume around *OTN-3* showed a minimum moment magnitude of  $M_W = -0.69$ . The largest observed magnitude was  $M_W = 1.54$  for the absolute located post-stimulation events. The subset of 1,987 relocated events showed moment magnitudes between  $M_W = -0.49$  and  $M_W = 1.87$ . The 70 relocated post-stimulation events had a minimum magnitude of  $M_W = -0.07$ .

### **3.2 Relocated catalog**

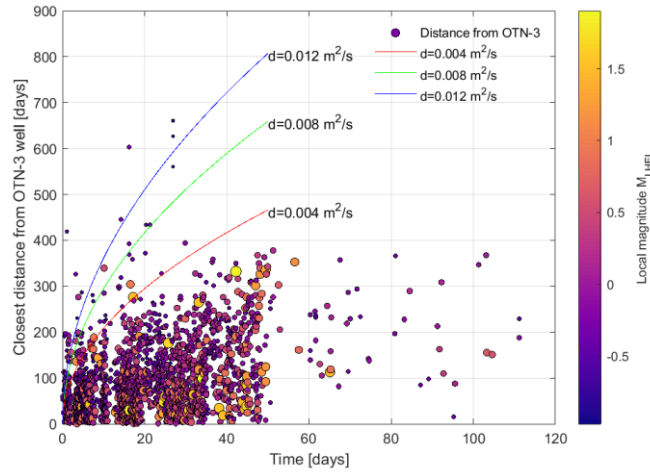
Figure 2 presents the relocated seismicity which occurred in three spatially separated clusters elongated in southeast (SE) - northwest (NW) direction and centered along the injection well, in good agreement with Kwiatek et al. (2019). Elongation of the clusters in SE-NW direction is sub-parallel to the local maximum horizontal stress  $S_H^{\max} = 110^\circ$  (Kwiatek et al., 2019). Further details about the relocated seismicity are discussed in Leonhardt et al. (2020).



**Figure 2.** Hypocenters of relocated events. (a) Map view and (b) SW-NE depth section. The hypocenters are color-coded with the stimulation phases (cf. Kwiatek et al., 2019) and size corresponds to moment magnitude. Relocated seismicity that occurred after the stimulation is represented as grey dots. The five injection stages are marked as color bands along the borehole trace from the bottom of the open-hole toward the casing shoe of the injection well *OTN-3* (black). The new *OTN-2* well (grey) was drilled in 2019 to 2020 after the stimulation.

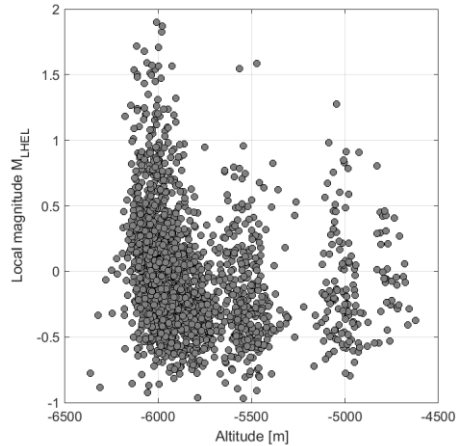
### 3.3 Spatio-temporal characteristics

Figure 3 shows the development of the seismicity with the horizontal distance from injection well *OTN-3*. This shows quick expansion of seismicity in lateral direction (mostly along SE-NW direction) in first two stimulation phases P1-P2 lasting 20 days (cf. Kwiatek et al., 2019), where the injection rates and injection well head pressures were the highest (cf. Kwiatek et al., 2019; Leonhardt et al., 2020). In following stimulation phases P3-P5, the expansion is slower and the seismicity front reaches approx. 400 m horizontal distance from *OTN-3* well. The post-stimulation phase displays no signatures in propagation with scattered seismicity confined to 400 m horizontal distance from *OTN-3* well.



**Figure 3.** Spatial development of the seismicity with time during *OTN-3* stimulation (until day 49) and in post-stimulation phase (from day 49). For each event, the distance is calculated as a distance between earthquake epicenter (EASTING, NORTHING) and the coordinate of the *OTN-3* well (EASTING, NORTHING) at the depth of earthquake (horizontal distance). The red, blue and green curves represent expected space-time evolution of a fluid pressure perturbation front triggering seismicity assuming that it is solely controlled by scalar fluid pressure diffusion in a homogeneous isotropic medium (e.g. Shapiro et al., 2020).

Figure 4 presents the dependence between earthquake depth and local magnitude. The figure marks the three distinct clusters of seismicity (cf. Fig. 2) developed during hydraulic stimulation. Largest seismic events as well as the highest level of seismic activity is observed in the lowermost cluster. This is expected due to expected elevated pore fluid pressures in the direct vicinity of injection activities, suggesting the seismic activity, as well as maximum magnitude is pressure-controlled (cf. discussion in Kwiatek et al., 2019; Bentz et al., 2020; Wang et al., 2020a, 2020b).



**Figure 4.** Dependence between earthquake depth (here presented as altitude a.s.l.) and local magnitude.

### 3.4 Gutenberg-Richter distribution

The catalog combining locations and detections displays  $b = 1.25$  with magnitude of completeness  $M_C = -1.10$  (Figure 5). Above  $M_{LHEL} 1.5$  the statistically significant roll-off is visible which was attributed to either geometrical constraint on pre-existing fracture network or limitation to fault strength (cf. Kwiatek et al., 2019). We note that although the magnitude of completeness of the full catalog is  $M_C = -1.10$ , the day-night cycles and associated anthropogenic noises reduces the completeness by approx. 0.2 (cf. Figure 2 in Kwiatek et al. (2019) where day-night cycle is clearly visible).

However, processing of events with  $M_{LHEL} < -0.7$  should be performed with caution. In a pending study (G. Kwiatek – pers. comm.) we note local magnitude estimates of small events with  $M_{LHEL} < -0.7$  are affected by high-frequency noises above 60 Hz (multiple resonance peaks) observed on sensors forming the vertical array in *OTN-2* well. The origin of these noises has been correlated to technological activities at the injection site, with the most likely noise source attributed to the high-performance injection pumps, as the noise seem to be correlation to injection rates. As recordings from *OTN-2* arrays are used to calculate local magnitude of smaller events that are not detected using the sensors close to the surface, and the local magnitude is calculated from integrated ground displacement seismograms which further emphasize the (temporary varying and resonant) noises, we expect significant bias in estimates of  $M_{LHEL}$  for  $M_{LHEL} < -0.7$ . This may lead to potential problems while analyzing statistical properties of induced seismicity such as magnitude correlations and or inter-event time statistics, to name a few. We suggest  $M_C = -0.7$  as a safe magnitude threshold that is not affected by noises originating from technological activity and day-night cycles. The subject is a topic of pending study (G. Kwiatek – pers. comm.) and this document will be updated accordingly when new information becomes available.

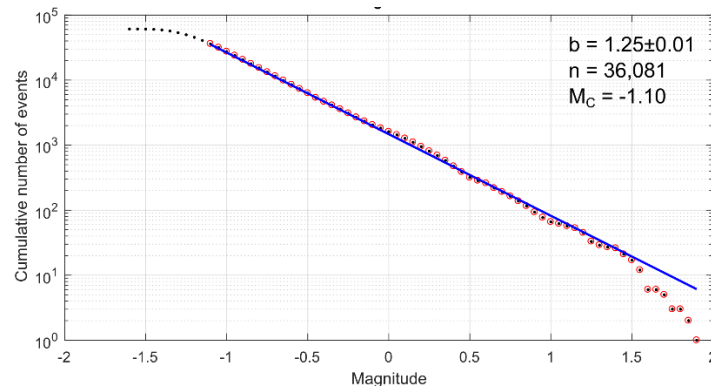


**Figure 5.** Magnitude-frequency relation for the entire seismic catalog analyzed in Leonhardt et al. (2020).

## References

- Bentz, S., Kwiątek, G., Martínez-Garzón, P., Bohnhoff, M., and Dresen, G.: Seismic moment evolution during hydraulic stimulations, *Geophysical Research Letters*, 47, e2019GL086185, <https://doi.org/10.1029/2019GL086185>, 2019.
- Efron, B.: *The jackknife, the bootstrap, and other resampling plans*, Siam, 1982.
- Font, Y., Kao, H., Lallemand, S., Liu, C.-S., and Chiao, L.-Y.: Hypocentre determination offshore of eastern Taiwan using the maximum intersection method, *Geophysical Journal International*, 158, 655–675, <https://doi.org/10.1111/j.1365-246X.2004.02317.x>, 2004.
- Hanks, T.C. and Kanamori, H.: A moment magnitude scale, *Journal of Geophysical Research: Solid Earth*, 84, 2348–2350, <https://doi.org/10.1029/JB084iB05p02348>, 1979.
- Hillers, G., Vuorinen, T., Uski, M., Kortström, J., Mäntyniemi, P., Tiira, T., Malin, P., and Saarno, T.: The 2018 geothermal reservoir stimulation in Espoo/Helsinki, Southern Finland: Seismic network anatomy and data features, *Seismological Research Letters*, 91 (2A), 770–786, <https://doi.org/10.1785/0220190253>, 2020.
- Kwiątek, G., Saarno, T., Ader, T., Bluemle, F., Bohnhoff, M., Chendorain, M., Dresen, G., Heikkinen, P., Kukkonen, I., Leary, P., Leonhardt, M., Malin, P., Martínez-Garzón, P., Passmore, K., Passmore, P., Valenzuela, S., and Wollin, C.: Controlling fluid-induced seismicity during a 6.1-km-deep geothermal stimulation in Finland, *Science Advances*, 5, eaav7224, <https://doi.org/10.1126/sciadv.aav7224>, 2019.
- Lagarias, J.C., Reeds, J.A., Wright, M.H., and Wright, P.E.: Convergence properties of the Nelder–Mead simplex method in low dimensions, *SIAM J. Optim.*, 9, 112–147, <https://doi.org/10.1137/S1052623496303470>, 1998.

- Leonhardt, M., Kwiatek, G., Martínez-Garzón, P., Bohnhoff, M., Saarno, T., Heikkinen, P., and Dresen, G.: Seismicity during and after stimulation of a 6.1 km deep enhanced geothermal system in Helsinki, Finland, *Solid Earth Discuss.*, <https://doi.org/10.5194/se-2020-139>, in review, 2020.
- Lomax, A.: A reanalysis of the hypocentral location and related observations for the great 1906 California earthquake, *Bulletin of the Seismological Society of America*, 95, 861–877, <https://doi.org/10.1785/0120040141>, 2005.
- Nelder, J.A. and Mead, R.: A simplex method for function minimization, *The Computer Journal*, 7, 308–313, <https://doi.org/10.1093/comjnl/7.4.308>, 1965.
- Shapiro, S. A., Rothert, E., Rath, V., and Rindschwentner, J.: Characterization of fluid transport properties of reservoirs using induced microseismicity, *Geophysics*, 67(1), 212–220, <https://doi.org/10.1190/1.1451597>, 2020.
- Uski, M. and Tuppurainen, A.: A new local magnitude scale for the Finnish seismic network, *Tectonophysics*, 261, 23–37, [https://doi.org/10.1016/0040-1951\(96\)00054-6](https://doi.org/10.1016/0040-1951(96)00054-6), 1996.
- Uski, M., Lund, B., and Oinonen, K.: Scaling relations for homogeneous moment based magnitude, in: *Evaluating seismic hazard for the Hanhikivi nuclear power plant site. Seismological characteristics of the seismic source areas, attenuation of seismic signal, and probabilistic analysis of seismic hazard*, edited by: Saari, J., Lund, B., Malm, M., Mäntyniemi, P., Oinonen, K., Tiira, T., Uski, M., and Vuorinen, T., (Report NE-4459, ÅF-Consult Ltd.), 125 pp., 2015.
- Waldhauser, F. and Ellsworth, W.L.: A double-difference earthquake location algorithm: Method and application to the Northern Hayward Fault, California, *Bulletin of the Seismological Society of America*, 90, 1353–1368, <https://doi.org/10.1785/0120000006>, 2000.
- Wang, L., Kwiatek, G., Rybacki, E., Bohnhoff, M., and Dresen, G.: Injection-induced seismic moment release and Laboratory fault slip: Implications for fluid-induced seismicity, *Geophysical Research Letters*, 47, e2020GL089576, <https://doi.org/10.1029/2020GL089576>, 2020a.
- Wang, L., Kwiatek, G., Rybacki, E., Bonnelye, A., Bohnhoff, M., and Dresen, G.: Laboratory study on fluid-induced fault slip behavior: The role of fluid pressurization rate, *Geophysical Research Letters*, 47, e2019GL086627, <https://doi.org/10.1029/2019GL086627>, 2020b.
- Wiemer, S. and Wyss, M.: Minimum magnitude of completeness in earthquake catalogs: Examples from Alaska, the Western United States & Japan, *Bull. Seismol. Soc. Am.*, 90, 859–869, <https://doi.org/10.1785/0119990114>, 2000.
- Zhou, H.: Rapid three-dimensional hypocentral determination using a master station method, *Journal of Geophysical Research: Solid Earth*, 99, 15439–15455, <https://doi.org/10.1029/94JB00934>, 1994.